

Reply to Reviewer 1:

1. General comments.

This paper presents a study including detailed analyses of ground-based observation data for snow precipitation events and a Bayesian retrieval results at GPM GMI channels. I'd like to add value to this study in providing additional information on observational characteristics of snow events, which has been challenging and generally not sufficient for both numerical modeling and satellite retrieval. The data and results are overall well organized and described, but there are some parts which need further clarifications and corrections for publication. Specific questions/comments I would suggest are below.

Thank you for your comments and suggestions. Your comments are very helpful. We made corrections and clarifications based on these comments (original comments in *italic*). Additionally, some revisions are also made based on comments from a discussion contributor, mainly related to radar reflectivity correction. In the revised version, radar reflectivity has been corrected for atmosphere and liquid water absorption (attenuation due to ice scattering has readily been corrected by processing software). While detailed numbers are revised in several figures, the main conclusions remain unchanged.

2. Specific comments.

Line 23: Specify the region of the study. Different regions may show different snow characteristics.

Indeed, the characteristics are region-dependent. We added the phrase “over Pyeongchang area in the east coast of the Korean Peninsula”.

Line107-110: What does it exactly mean by this? Still explaining the Bayesian algorithms? Please clarify.

Yes, here we are still explaining Bayesian algorithms. To clarify, this sentence is rewritten as: “The snowfall rates in a Bayesian algorithm database are often retrievals from radars and the brightness temperatures are either those collocated measurements of passive microwave radiometers or simulated by radiative transfer models.”

Line 135: It would be helpful for readers to specify the greatest DTB, and the thresholds for each very shallow or very deep.

This sentence is revised as: “The results show that the discrepancy between simulated and observed brightness temperatures is the greatest for very shallow (cloud top around 2 km) or very deep (cloud top around 8 km) snowing clouds with discrepancy value being over 10 K in the former and over 30 K in the latter case, although it is generally less than 3 K when averaged over all selected pixels under snowfall conditions.”

Line 139: Please clarify the sentence. Add more explanation if needed.

This sentence is revised as: “For very shallow snowing clouds, cloud liquid water may be rich and contributes substantially to the observed brightness temperatures. However, the radiative transfer model, which uses CloudSat radar and GMI retrievals as input, failed to account for this liquid water abundance, resulting in a large discrepancy between simulated and observed brightness temperatures.”

*Line 145 One additional sentence would be desirable to explain an object of the field study. &
Line 146: Any reference for ICE-POP?*

A sentence and a reference are added. “The experiment focuses on the measurement, physics, and improved prediction of heavy orographic snow in the PyeongChang region of South Korea (Gehring et al., 2020).”

Line 152-153: This study also includes a Bayesian retrieval for GPM GMI, not just to analyze the observational measurements. Any additional goal to emphasize the value of this study?

A new sentence is added. “Furthermore, we examine how a Bayesian snowfall retrieval algorithm with GPM/GMI observations would perform for the snowing clouds observed during this field experiment.”

Eq.(1): No need to adjust for snow events over Korea, and specifically for 94 GHz cloud radar?

This equation was originally derived for CloudSat radar which has the same frequency (94 GHz) as this surface radar. So, adjustment for frequency is not needed. However, adjustment for snow events over Korea is an open question. The particle shapes and size distributions used for deriving Eq.(1) will differ from those in snow events over Korea. But it is difficult to know how they differ. So, uncertainties will be associated with using this equation. We added one sentence to mention this issue. “It should be mentioned that although Eq.(1) is developed for CloudSat radar which has the same frequency as the RPG-FMCW radar, uncertainties in particle shapes and size distributions will certainly cause errors in snow water content derived in this study.”

Line 205-206: How to derive T_c . How is it considering the cloud base?

We derived T_c by the air temperature at the height of the geometric middle of radar reflectivity profiles. In other word, cloud base is assumed to be the lowest level with valid radar echo. In case of snowfall, it is assumed to be the ground. A sentence is added to describe this derivation. “which [T_c] is determined in this study by the air temperature at the height of the geometric middle of valid radar reflectivity profiles.”

Line 238: 0.1 m/s is only in this case or averaged from multiple cases?

It is an average for multiple cases. We examined this and some other cases, and found 0.1 m/s is a reasonable threshold to determine cloud top. This exemplar case is given here to show how this threshold worked.

Line 244: "While quantitative analysis was not ..." -> How do you expect this could impact on the results and future improvement (in conclusions)?

Particle shapes definitely are useful information in understanding microphysics and improving retrieval algorithms. These data are treasures to be explored in the future. We added some discussions in the last (conclusions) section. "Lastly, it is worth mentioning that there are still many valuable datasets, such as particle shape and size distribution information from PARSIVEL, 2DVD and MASC, which we didn't analyzed quantitatively in this study. A thorough analysis of those datasets in conjunction with the remote sensing data will undoubtedly improve future snowfall retrieval algorithm development."

Line 266: "A common radar..." -> Any previous studies? & Line 268: Any references to determine snow event types over this region?

This paragraph is completely rewritten. We added a summary of synoptic patterns for snowfall in the Pyeongchang area and their associated snow clouds types. A number of references are also provided. The deep clouds are commonly associated with low pressure systems, and the shallower clouds are associated with convective cells. The revised paragraph is as follows. "There are several synoptic weather patterns that cause snowfall over the Pyeongchang area. The first pattern is a synoptic low pressure system, so-called "cold low", developed over the Yellow sea (west of Korea) or cold continent and causes the snowfall over the northern or middle part of Korea when moving to east (Chung et al. 2006; Ko et al. 2016; Park et al. 2019). As this system crosses the Korean peninsula, the system become weaker and shallower once moving over the Pyeongchang area. The precipitation intensity and depth of system depend on the strength of low pressure. The second synoptic pattern, "warm low," develops over the warm ocean near East China sea or South sea and moves to north-east or east (Nam et al. 2014; Gehring et al 2020). This synoptic pattern brings abundant moisture to Korean Peninsula and is typically favored for vertically well-developed precipitation system. As the warm low pressure passes the Korean Peninsula and East sea, the winds over the Pyeongchang area and East sea turns to easterly or north-easterly, bringing in cold air to the east coastal area. Thus, we expect that the depth of precipitation system is likely first deep with large moisture and later becomes shallower as influenced by north-easterly cold air. The third interesting pattern, so-called "air-sea interaction", is developed by the easterly or north-easterly flow due to the Kaema high over the northern mountain complex or high pressure over Manchuria by the eastward expansion of the Siberian high (Kim and Jin 2016; Kim et al 2019). Thus, the cold north-easterly or easterly flow enhances the interaction with warm moisture ocean, resulting in the development of shallow convection and thermal inversion in the lower troposphere. The shallow convective clouds move to the coastal and mountain area where they are lifted by the orography. An example of radar reflectivity cross section is shown in Fig.1 where deeper clouds lead to shallower convective cells. This is the case of the second synoptic type, warm low. During the passage of the warm low, the system reached to 9 km. However, the precipitation system is shallower than 1 km during easterly or north-easterly flow when the warm low pressure passed the East sea."

Line 291: -20 dBZ -> with that, light snow events can be yet counted sufficiently?

Based on studies we know so far, -20 dBZ is a quite a low threshold. We added 2 sentences and a reference here to justify this threshold. “In a study by Wang et al. (2017) based on CloudSat radar reflectivity profiles, they found that precipitation onset often occurs when radar reflectivity is about -18 to -13 dBZ. We use the value of -20 dBZ as criterion in this study to make sure that all possible snowfall cases are included in the precipitation samples.”

Line 294-295: Need more details about samples collected during the field experiment (such as the numbers basically as written in the conclusion part).

This paragraph is rewritten to give info of the samples and the ways how the fractions are calculated. The revised text is as follows.

“Surveying all observed data for the entire winter, approximately 374 hours of observations are deemed as snowfall events after we apply the -20 dBZ threshold at the lowest bin and the Sims and Liu (2015) algorithm to exclude rain events. These observations are then averaged over each 5-minute interval to form 4491 samples. The relative frequencies of occurrence (area fraction, calculated by the number of samples of a given snow type divided by the total number of snowfall samples) and snowfall amount (volume fraction, calculated by the snowfall amount produced by a given snow type divided by the total snowfall amount by all types) for the three types of snowing clouds are shown in Fig.3. The snowfall volume is the accumulated snowfall with the rate estimated by Eq.(2) from radar reflectivity at the lowest bin. Over half (67.4%) of the observed samples are near-surface snowfall, followed by shallow (21.2%) and then deep (11.4%) snowing clouds. However, deep snowing clouds contribute the most to the total snowfall volume (45.3%), followed by shallow (28.5%) and then near-surface (26.2%) snowing clouds.”

Line 427-428: Are those averaged profiles from observed samples?

Yes. We revised this sentence to clarify. “Note that in these radiative transfer calculations, mean snowfall rate profiles derived from observations are used. The mean profiles are derived as follows. We first group all the observed snowfall rate profiles according to their cloud type, and then for each cloud type we average those profiles that fall into a given snowfall rate bin.”

Line 429: The heights to place the liquid layer are right above the snow cloud layer?

Actually, the liquid layer is within the snow cloud layer, but closer to the top part of the snow cloud layer. We assume the clouds are mixed phase clouds with the liquid embedded in the upper portion of the cloud layers.

Line 433-434: Add the decreased TB values.

This sentence is revised. “ ..., only about 1.5 K for 89 GHz and 2.5 K for 166 GHz occurring when liquid water path is very low.”

Line 544-545: Please make it clear that this is for the cases studied here or particularly over the target region in this study.

We added “In this region during the observation period,” to clarify.

Line 571: What it means exactly? The half of a priori database was from model simulations?

This part is rewritten to make the meaning clear. Now it reads: “Moreover, we examined the ability of a Bayesian type algorithm to retrieve surface snowfall rate for snow events similar to those observed in this study when using GPM/GMI observations. First, using the approximately 30,000 observed snow cloud and precipitation-free profiles, brightness temperatures at GPM/GMI channels are computed. Then, these snowfall rate and associated brightness temperature pairs are randomly divided into two equal-number groups. One group is used as “observations” and the other is used as the *a priori* database of the Bayesian algorithm.”

3. Technical corrections.

Line 288: Add year.

Line 556: with vast majority of “them”

Line 570: half “of”

All are corrected as suggested. Thank you.

Reply to Reviewer #2

General comments:

Thank you for your constructive comments and suggestions. We revised the manuscript based on your comments and suggestions. The following are responses to your specific comments (original comments in *italic*). Additionally, some revisions are also made based on comments from a discussion contributor, mainly related to radar reflectivity correction. In the revised version, radar reflectivity has been corrected for atmosphere and liquid water absorption (attenuation due to ice scattering has readily been corrected by processing software). While detailed numbers are revised in several figures, the main conclusions remain unchanged.

Specific comments:

How generalized are the findings and conclusions? For instance, Kulie (2016) found that shallow snow cloud can be associated with strong convection and heavy snowfall while almost all the shallow (and near-surface) snowfall in this study is less than 0.5 mm/hr (Fig.6). Please add some discussions to answer this question.

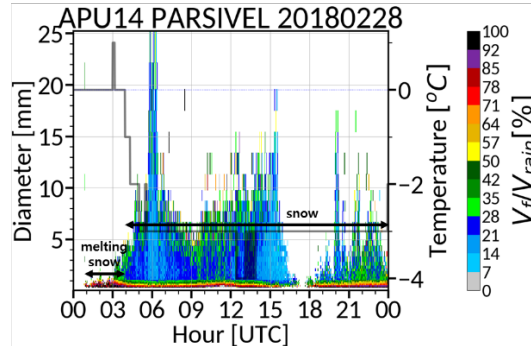
We added that following discussions in section 4.2: “Kulie et al. (2016) found that globally shallow snow clouds can be associated with strong convections and heavy snowfall. The snowfall rates for shallow and near-surface snow clouds observed in this study are mostly lower than 0.5 mm h^{-1} ; heavy snowfall is mainly associated with deep snow clouds. One possible explanation of the difference is as follows. The snowfall from shallow and near-surface snow clouds in this study mostly comes from convections associated with cold airmass outbreak from the northwest. Since the observation site is in the mountains in the east coastal region of the Korean Peninsula, substantial portion of the moisture picked up by the cold air from the warm ocean in the Yellow Sea (west of the Korean Peninsula) has been already transformed to snow before reaching the observation site. In addition, the convective clouds and easterly flow can cross the mountains and produce heavy snowfall over the site in the case of strong winds and lower thermal stability. However, these types of events occurred relatively infrequently during the experiment when compared to the other snowfall types. Consequently, the snowfall associated with shallow and near-surface clouds at this site is relatively moderate.”

-Line 279: Add a sentence about the common cause of near-surface snowfall. Is it usually convective?

The following sentence is added: “Similar to the case of shallow snow clouds, the near-surface snow clouds also mostly occur after front passing or during north-easterly/easterly flow, and are convective in nature.”

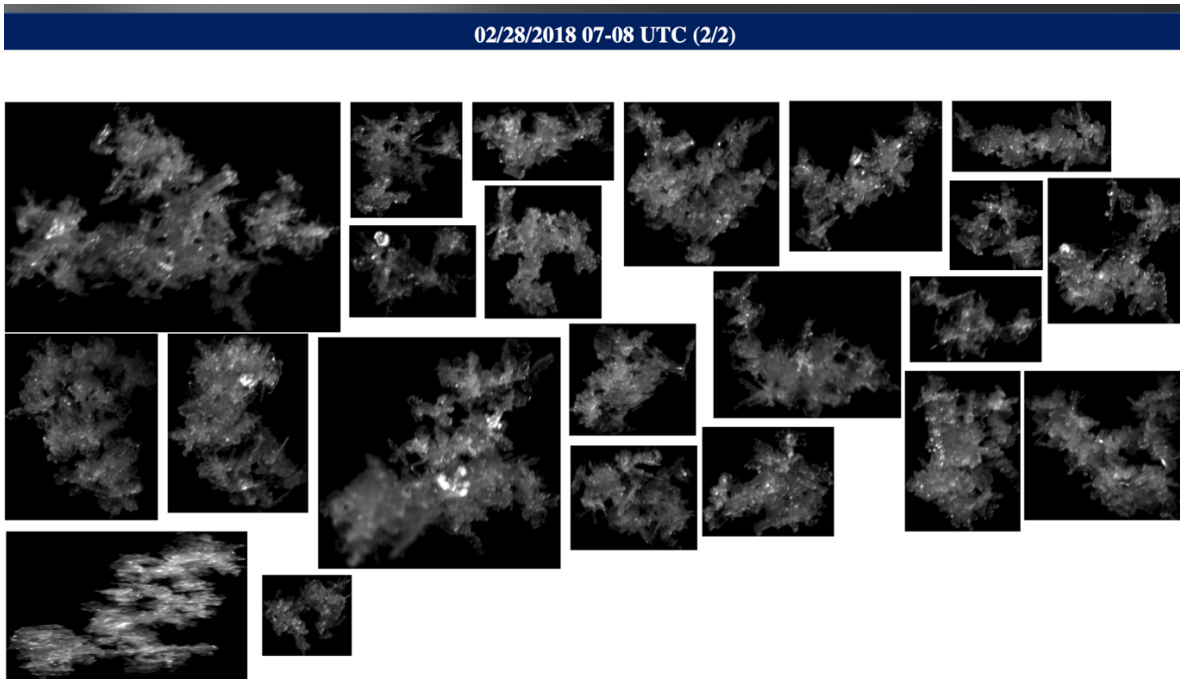
-Line 320: What caused melting snow? What’s the temperature profile like?

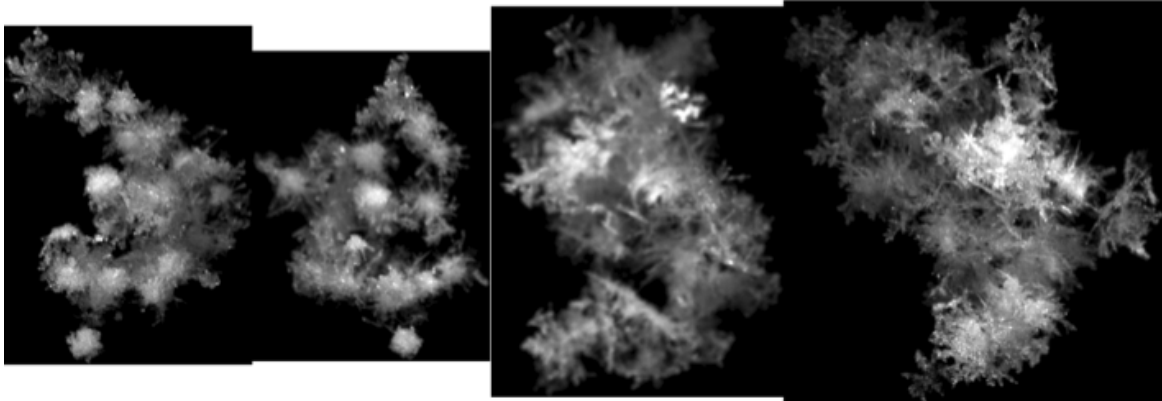
The melting is caused by temperature near 0°C . See the PARSIVEL data below. Surface temperature is solid line with axis on the right. We added “with surface air temperature near 0°C ” in the sentence.



-Line 321-325: Was riming also occurring during heavy snowfall? LWP was quite high at the time.

The following are MASC pictures measured at 05-06UTC and around 20-21UTC. Both are large fluffy flakes, and seemed to show some riming. A phrase “snowflakes observed at surface are large aggregates and show indications of riming occurred” is added.





-Line 356-359 The conclusion might be partially true for reflectivity between 2 and 10 but it's not universal. It looks to me that Fig. 8(b) mainly shows high LWP associated with large surface reflectivity, i.e. heavy snowfall. The text needs to be modified. & Line 359-361: Again, the conclusion is not universal, and the text needs to be modified.

This paragraph is rewritten as follows.

“The diagrams for mean and standard deviation of liquid water path shown in Figs.8b and 8c appear to indicate the following. For deep snow clouds (top higher than 4 km) with surface radar reflectivity greater than 6 dBZ, liquid water path has a large mean value but a small standard deviation. On the other hand, shallow snow clouds (top between 1.5 and 4 km) with moderate surface radar reflectivity (0-5 dBZ) have a moderate mean value but a high variability of liquid water path. There is an area with high mean value and high variability of liquid water path located at surface radar reflectivity between -10 and 0 dBZ and cloud top height between 4 and 6 km, possibly corresponding to convective cells in early developing stage. For near-surface and shallow clouds, both the mean value and standard deviation of liquid water path appear to increase as surface radar reflectivity increases.”

-Lines 368-370: It's interesting that Fig.9(a) shows a concentration of data with high cloud top heights (>5 km) but GR between 50%-75% rather than close to 100%. Can you add some comments about the phenomena and maybe its cause?

We suspected that this may be caused by clouds with multiple layers or decoupled upper and lower layers. The following sentence is added. “In Fig.9a, there is a concentration of points with high cloud top (>5 km) but glaciation ratio between 50% and 75% rather than 100%. It is likely that the phenomena are caused by clouds that have multiple layers or a cloud layer with dynamically decoupled upper and lower portions”

-Line397-398: There is a shift in this tendency at 4km for deep snowing clouds: fall velocity becomes slower at 4km. There also seems a shift in the spectral width at this height. Is there an explanation for it? What's the significance of this height?

Interesting observation. In fact, the radar reflectivity CFADs also shows the shift near 4 km – below it, the frequency shows a vertical pattern while above it a left-leaning pattern. This seems to indicate the main precipitation growth occurs above 4 km. It must be related to large-scale updraft, namely, on average, bulk of the updraft occurs above 4 km in these deep clouds. We added a few sentences to describe this phenomenon. “It is also interesting to notice that there seems to be a regime shift for deep snow clouds near 4 km altitude; the frequency patterns appear to be different below and above this level for all the CFADs of radar reflectivity, Doppler velocity and spectrum width. Additionally, the slope of reflectivity suddenly changes around 8 km and the absolute value of Doppler velocity reduced dramatically below 8 km. A similar feature also appeared in the long-term observation with cloud radar (see Figs. 16 and 17 of Ye et al. 2020). The shift of growth regime was appeared at 8 km height (3~3.5 km above the bright band peak and corresponding to ~ -17 °C). This regime shift induced the updraft (reached 1 m s^{-1}) below this layer. However, Ye et al. (2020) could not explain the linkage between this regime shift and updraft below. While it is beyond the scope of this study, this phenomenon will be an interesting topic for future research on the cloud microphysics in this region.”

-Line 445-446: Liquid water also has an impact on deep snowing clouds (Fig. 11 c and f) so underestimation is likely for this type of snowfall. Depending on the algorithm, overestimation is also possible for clouds with low LWP. This can be seen in Fig. 12(c) where S is overestimated below 0.2 mm/hr for low LWP. Suggest modifying this sentence accordingly.

You are right. This sentence is modified as “Even for deep snowing clouds, cloud liquid water will impact snowfall retrieval with a result of an overestimation for low and an underestimation for high values of liquid water path.”

-Figures 12 and 13: S is mostly underestimated if measured S is greater than about 0.7 mm/hr in deep snowing clouds. Please add some discussions about it.

A paragraph is added to discuss this problem. “In Figs. 12 and 13, it is also noted that an underestimation occurs when snowfall rate is greater than 0.7 mm h^{-1} for deep snowing clouds regardless over land or ocean. This underestimation may be due to the deficiency of the Bayesian scheme, in which the retrieval is a weighted average of snowfall rates of datum points in the a priori database that are radiometrically consistent with observations. When an observation is close to the upper boundary (i.e., high snowfall rates) in the database, the averaging takes a greater number of datum points with snowfall rates lower than the actual value than those with higher snowfall rates (no more datum points beyond upper boundary), thus resulting in an underestimation.”

-Figures 12 and 13: Besides R2, also calculate bias and RMS for the evaluation of retrievals.

Bias and rms are calculated and the values are added in the figures and text.

-Line 492-496: I can't fully agree with the statements here. First, low LWP (<50) snowfall is underestimated for near-surface snowing clouds but overestimated at the low end for deep snowing clouds so the magnitude of LWP does make a difference. Secondly, this study has shown

that the type of snowfall (defined by cloud depth) instead of snowfall rate that has a significant impact on the retrieval skills.

You are right. This statement is not supported by the results. Because this is not a major point we want to make, we decide to delete this sentence.

Technical corrections:

- *Lines 381-382: There are no (a), (b), and (c) in Fig. 10. Needs to be consistent with the figure caption. / (a,b,c □ top, middle, bottom)*
- *Line 471: Change 'merely sensible' to 'not sensitive'.*
- *Figure 12: Make (a) and (b) larger even if the axis ranges will be different from (c). Same with Fig. 13.*

All are corrected as suggested. Figs.12 and 13 are replotted. Thank you.

1 **Microphysical Properties of Three Types of Snow Clouds: Implication to Satellite**
2 **Snowfall Retrievals**

3

4 Hwayoung Jeoung¹, Guosheng Liu¹, Kwonil Kim², Gyuwon Lee², and Eun-Kyoung Seo³

5

6 1. Department of Earth, Ocean and Atmospheric Science, Florida State University,
7 Tallahassee, Florida, U.S.A.

8 2. Department of Astronomy and Atmospheric Sciences, Center for Atmospheric
9 REmote Sensing (CARE), Kyungpook National University, Daegu 41566,
10 Republic of Korea

11 3. Department of Earth Science Education, Kongju National University, Kongju
12 314-701, Republic of Korea

13

14

15

16

17

18

19 Submitted to ACP, ICE-POP Special Issue ([revised October 2020](#))

20

Abstract

Ground-based radar and radiometer data observed during the 2017-18 winter season over Pyeongchang area in the east coast of the Korean Peninsula were used to simultaneously estimate both cloud liquid water path and snowfall rate for three types of snowing clouds: near-surface, shallow and deep. Surveying all the observed data, it is found that near-surface cloud is the most frequently observed cloud type with an area fraction of over 60%, while deep cloud contributes the most in snowfall volume with about 50% of the total. The probability distributions of snowfall rates are clearly different among the three types of clouds, with vast majority hardly reaching to 0.3 mm h⁻¹ (liquid water equivalent snowfall rate) for near-surface, 0.5 mm h⁻¹ for shallow, and 1 mm h⁻¹ for deep clouds. However, liquid water path in the three types of clouds all has substantial probability to reach 500 g m⁻². There is no clear correlation found between snowfall rate and liquid water path for any of the cloud types. Based on all observed snow profiles, brightness temperatures at Global Precipitation Measurement Microwave Imager channels are simulated, and the ability of a Bayesian algorithm to retrieve snowfall rate is examined using half the profiles as observations and the other half as *a priori* database. Under idealized scenario, i.e., without considering the uncertainties caused by surface emissivity, ice particle size distribution and particle shape, the study found that the correlation as expressed by R² between the “retrieved” and “observed” snowfall rates is about 0.32, 0.41 and 0.62, respectively, for near-surface, shallow and deep snowing clouds over land surface; these numbers basically indicate the upper limits capped by cloud natural variability, to which the retrieval skill of a Bayesian retrieval algorithm can reach. A hypothetical retrieval for the same clouds but over ocean is also studied, and a major improvement in skills is found for near-surface clouds with R² increased from 0.32 to 0.52, while smaller improvement is found for shallow and deep clouds. This study provides a general picture of the microphysical characteristics of the different types of snowing clouds and points out the associated challenges in retrieving their snowfall rate from passive microwave observations.

Formatted: Justified, Indent: First line: 0.5", Space After: 8 pt

Deleted: 33

Deleted: 48

Deleted: 74

Deleted: 33

Deleted: 54

Deleted: virtually no change

Deleted: in skills

Deleted: deep

Deleted: and only marginal improvement is found for shallow clouds.

Deleted: ¶

62 1. Introduction

63

64 Snowfall is an important component in the global hydrological cycle. Its global
65 distribution may be observed using satellite-based passive and active microwave sensors.
66 Currently, there are multiple satellites in operation carrying passive microwave sensors that
67 are potentially able to be used for snowfall observations, which offers great spatial and
68 temporal coverages for various snowfall related studies. Meanwhile, while only a few
69 spaceborne active sensors are currently available for snowfall observations, they have the
70 advantage of providing information on the vertical structure of precipitation. Nevertheless,
71 whether active or passive sensors are used, in order to convert the observed radiative
72 signatures (brightness temperature or radar reflectivity) to snowfall rate, two factors related
73 to the snowing clouds play an essential role: one is the vertical extent of the cloud layer
74 and the other is the cloud microphysical properties such as particles' phase and amount.
75 Using ground-based observations from multiple sensors, in this study we intend to
76 understand these properties for three distinctive types of snowing clouds. By performing
77 radiative transfer simulations, we further investigate the implication of the variability in
78 microphysical properties to satellite snowfall retrievals from passive microwave
79 observations.

80 Snowfall retrieval has been investigated recently for both active and passive
81 satellite measurements. The cloud radar onboard CloudSat satellite (Stephens et al., 2002;
82 Tanelli et al., 2008) is the first spaceborne active sensor in operation that is suitable for
83 snowfall observations. It has a minimum detectability of near -30 dBZ near the ground,
84 allowing to observe the weak scattering signal from snowflakes. Kulie et al. (2016) used
85 CloudSat cloud classification and snowfall rate retrievals to partition snowfall observations
86 into shallow cumuliform and deep nimbostratus snowfall categories. Their results show
87 that there are abundant shallow snow cloud cells globally and they can be associated with
88 strong convection and heavy snowfall. For example, they found that shallow snowfall
89 comprises about 36% in the 2006–10 CloudSat snowfall dataset by occurrence, while
90 constituting some 18% of the estimated annual global snowfall accumulation. Shallow
91 precipitation can be easily missed by space-borne radars. Although CloudSat radar
92 provides information on the vertical structure of precipitation, there is a blind zone below

93 about 1.5 km due to ground clutter contamination. In most analysis, the lowest range bin
94 (bin depth is ~240 m) where radar data are not contaminated by surface clutter is often the
95 third (fifth) above the actual surface over oceanic (land) surfaces (Wood et al., 2013; Kulie
96 and Bennartz, 2009; Liu, 2008a; Marchand et al., 2008). Hudak et al.(2008) studied the
97 ability of CloudSat radar to detect precipitation in cold season clouds using data from a C
98 band weather radar at King City, Ontario. They found that the most frequent cause of a
99 miss in detection by CloudSat radar was due to ground clutter removal of valid echoes by
100 the algorithm. Similarly, Chen et al. (2016) compared snowfall estimates from CloudSat
101 radar (Wood et al., 2013) and ground radar derived Multi-Radar and Multi-Sensor (MRMS)
102 product (Zhang et al., 2016), and found that the lowest height with valid estimate for most
103 (99.41%) snowfall events in CloudSat product is over 1 km above surface, whereas it for
104 76.41% of the corresponding MRMS observations is below 1 km.

105 Using satellite passive microwave observations at high frequency channels,
106 snowfall may be retrieved due to the scattering of upwelling radiation by snowflakes
107 (Katsumata et al., 2000; Bennartz and Bauer, 2003; Skofronick-Jackson and Johnson, 2011;
108 Gong and Wu, 2017). Retrieval algorithms have been developed both in research mode
109 (Kim et al., 2008; Kongoli et al., 2015; Liu and Seo, 2013; Noh et al., 2006; Skofronick-
110 Jackson et al., 2004) and for operations (Kummerow et al., 2015; Meng et al., 2017).
111 Skofronick-Jackson et al. (2004) and Kim et al. (2008) developed physically-based
112 retrieval algorithms which seek the best match between radiative transfer model simulated
113 and satellite observed brightness temperatures. The Liu and Seo (2013) and Kongoli et al.
114 (2015) algorithms are mostly statistical in which many pairs of radar and/or gauge-
115 measured snowfall and satellite measured brightness temperatures are used to develop their
116 statistical relations. The Noh et al. (2006) and Kummerow et al. (2015) snowfall algorithms
117 are based on the Bayesian theorem; an *a priori* database linking snowfall and brightness
118 temperatures needs to be prepared before conducting retrievals. The snowfall rates in a
119 Bayesian algorithm database are often retrievals from radars and the brightness
120 temperatures are either those collocated measurements of passive microwave radiometers
121 or simulated by radiative transfer models. The Meng et al. (2017) algorithm uses a one-
122 dimensional variational method to seek the consistency between measured brightness
123 temperatures and microphysical properties in the atmospheric column. Its performance has

Deleted: the

Deleted: is

Deleted: retrieved

Deleted: from

Deleted: by

129 been verified by surface radar and gauge observations over the U.S. with satisfactory
130 results.

131 Although the above successes have been achieved by previous investigators, there
132 are still large discrepancies among different snowfall retrievals (Casella et al., 2017;
133 Skofronick-Jackson et al., 2017; Tang et al., 2017). Algorithm uncertainty arises from
134 many factors; one of them is the insufficient knowledge of microphysical properties of the
135 snowing clouds, in particular, the amount of cloud liquid water. The increase in brightness
136 temperature over cloudy skies due to liquid water emission in snowing clouds complicates
137 the snowfall detection and retrieval problems (Liu and Curry, 1997; Liu and Seo, 2013;
138 Wang et al., 2013). Wang et al. (2013) showed that the warming by liquid water emission
139 has a similar magnitude to the cooling by ice scattering on microwave brightness
140 temperatures at frequencies higher than 80 GHz. Liu and Seo (2013) discovered a warming
141 rather than cooling signal in high-frequency brightness temperature in most snowfall cases
142 they analyzed.

143 In addition, correctly simulating brightness temperatures is needed for physical
144 snowfall retrievals as well as data assimilation of radiance observations in numerical
145 weather prediction models. Yin and Liu (2019) has studied the bias characteristics of
146 observed minus simulated brightness temperatures at high frequency channels of Global
147 Precipitation Measurement Microwave Imager (GPM/GMI) under snowfall conditions. In
148 their study, a radiative transfer model that includes single-scattering properties of non-
149 spherical snow particles is used to simulate brightness temperatures at 89 through 183 GHz.
150 The input snow water content profiles are derived from CloudSat radar measurements. The
151 results show that the discrepancy between simulated and observed brightness temperatures
152 is the greatest for very shallow (cloud top around 2 km) or very deep (cloud top around 8
153 km) snowing clouds with discrepancy value being over 10 K in the former and over 30 K
154 in the latter case, although it is generally less than 3 K when averaged over all selected
155 pixels under snowfall conditions. They explained the results as follows. For very shallow
156 snowing clouds, cloud liquid water may be rich and contributes substantially to the
157 observed brightness temperatures. However, the radiative transfer model, which uses
158 CloudSat radar and GMI retrievals as input, failed to account for this liquid water
159 abundance, resulting in a large discrepancy between simulated and observed brightness

Deleted: ,

Deleted: while

Deleted: inputs based on CloudSat radar retrievals

Deleted: .

163 temperatures. For very deep snowing clouds, they hypothesized that CloudSat radar
164 experiences substantial attenuation as well as non-Rayleigh scattering, which leads to
165 higher simulated brightness temperatures than observed. A better understanding of the
166 microphysical properties in very shallow and very deep snowing clouds is clearly needed
167 to reduce the discrepancies between simulated and observed brightness temperatures.

168 A field experiment was conducted over the Korean Peninsula during the winter of
169 2017-2018, coinciding with the 2018 winter Olympic Games (ICE-POP 2018:
170 International Collaborative Experiments for PyeongChang 2018 Olympic and Paralympic
171 Winter Games). The experiment focuses on the measurement, physics, and improved
172 prediction of heavy orographic snow in the Pyeongchang region of South Korea (Gehring
173 et al., 2020). During the field experiment, many ground-based observations including radar,
174 radiometer and *in situ* observations were conducted. In this study, we analyze the vertical
175 structure and microphysical properties of these snowing clouds, with focus on their
176 potential impacts on satellite remote sensing of snow precipitation. The main objective of
177 the study is to gain better understanding of the characteristics of snowing clouds that are
178 critical to satellite remote sensing of snowfall. Furthermore, we examine how a Bayesian
179 snowfall retrieval algorithm with GPM/GMI observations would perform for the snowing
180 clouds observed during this field experiment.

181

182 2. Data and Methods

183

184 2.1 Ground-based Cloud Radar and Radiometer

185 Observations from the Radiometer Physics GmbH-Frequency Modulated Continuous
186 Wave 94 GHz cloud radar (RPG-FMCW, 2015) are the primary data source for this study.
187 This vertical pointing radar is installed at 37.66°N, 128.70°E (altitude 735 m above sea
188 level) over Korean Peninsula during the ICE-POP 2018 field campaign. It has an operation
189 frequency of 94 GHz for radar backscatter and Doppler spectrum measurement and an
190 embedded 89 GHz passive channel for liquid water path measurement. It is noted that while
191 we refer this instrument as a cloud radar for convenience, it indeed includes an independent
192 passive microwave channel at 89 GHz, which is used for cloud liquid water estimation.
193 There is clearly an advantage of this instrument in studying the composition of cloud liquid

195 and ice over those that measure radar reflectivity and brightness temperature by two
196 separate instruments because this instrument measures emission and scattering signatures
197 from the same cloud volume, therefore, avoids beam mismatching problem by a separated
198 radar and radiometer. The vertical resolution of radar reflectivity measurement is selectable
199 from 1, 5, 10, or 30 m, with overall radar calibration accuracy better than 0.4 dB. The
200 minimum detectable radar reflectivity depends on the range and vertical resolution; at its
201 typical operation mode of 30 m resolution, it is -36 dBZ at 10 km height, which is
202 sufficiently sensitive for snowfall detection. In addition to radar reflectivity, the RPG-
203 FMCW also measures Doppler spectrum with a Doppler velocity resolution of 1.5 cm s⁻¹.

204 [A detailed explanation of the calibration of this instrument can be found in K uchler et al.](#)
205 [\(2017\).](#)

206 207 2.2 Retrieved Microphysical Variables

208
209 In this study, the radar reflectivity Z_e is converted to snow water content (SWC)
210 and snowfall rate (S) using the Z_e -SWC relation of Yin and Liu (2017) and Z_e -S relation
211 of Liu (2008a). [Before performing these conversions, radar reflectivity was corrected for](#)
212 [attenuation due to absorption by atmospheric gases and cloud liquid water, and scattering](#)
213 [by ice particles. Absorption by atmospheric gases is calculated based on Rosenkranz \(1998\)](#)
214 [for water vapor and Schwartz \(1998\) for oxygen with input of geophysical parameters](#)
215 [interpolated from the Modern Era Reanalysis for Research and Applications Version-2](#)
216 [\(MERRA-2\) \(Gelaro et al., 2017\). Absorption by cloud liquid water is computed using](#)
217 [liquid water path derived by the method described later in this section and assuming cloud](#)
218 [liquid water uniformly distributed vertically in the radar echo layer. Refractive index of](#)
219 [liquid water is calculated based on Liebe et al. \(1993\). Attenuation due to ice scattering](#)
220 [was readily performed by manufacture-provided processing software \(RPG-FMCW, 2015\).](#)

221 The Yin and Liu (2017) Z_e -SWC relation is given by

$$222 \quad \text{SWC} = 0.024Z_e^{0.75}, \quad (1)$$

223 where SWC is in g m⁻³ and Z_e is in mm⁶ m⁻³. In developing the above equation, three snow
224 particle types are employed: sectors, dendrites (Liu, 2008b), and oblate aggregates
225 (Honeyager et al., 2016). The backscatter cross sections of the three snowflake types are

Deleted: 's

227 computed using discrete dipole approximation (DDA) (Draine and Flatau, 1994; Liu, 2004).
228 It should be mentioned that although Eq.(1) is developed for CloudSat radar which has the
229 same frequency as the RPG-FMCW radar, uncertainties in particle shapes and size
230 distributions will certainly cause errors in snow water content derived in this study.

231 The Liu (2008a) S-Z_e relation is given by

$$Z_e = 11.5S^{1.25}, \quad (2)$$

232 where S is in mm h⁻¹ (liquid water equivalent snowfall rate) and Z_e is in mm⁶ m⁻³. The
233 backscatter cross sections in Eq.(2) are computed for rosettes, sectors and dendrites using
234 DDA (Liu, 2008b).

235
236 In addition to radar reflectivity, the mean Doppler velocity and spectral width, the
237 RPG-FMCW also measures brightness temperature at 89 GHz. While there is a liquid water
238 path (LWP) variable produced by the manufacture-provided software, details about the
239 liquid water path retrieval algorithm and its accuracy have not been well documented. In
240 this study, we chose to adapt the algorithm of Liu and Takeda (1988) in computing liquid
241 water path from 89 GHz brightness temperatures. Briefly, the brightness temperature T_B
242 received by an up-looking radiometer can be divided into two portions, i.e., the cloud-free
243 atmospheric emission and the liquid cloud water emission. The emissivity of the liquid
244 water cloud ε_c may then be approximated by

$$\varepsilon_c = \frac{T_a(T_B - T_{Ba})}{T_c(T_a - T_{Ba})}, \quad (3)$$

245
246 where T_a is a radiatively-mean temperature of the atmosphere in Kelvin, which can be
247 evaluated by absorption-coefficient-weighted averaging atmospheric temperatures in
248 vertical. Its value roughly equals to the temperature around 1.5 km altitude. T_c is the mean
249 temperature of the cloud layer, which is determined in this study by the air temperature at
250 the height of the geometric middle of valid radar reflectivity profiles. T_{Ba} is the brightness
251 temperature from the liquid-free atmosphere, which is derived using interpolation between
252 measured T_{BS} at echo-free regions in this study. From ε_c calculated from (3), liquid water
253 path (LWP) can be derived by

Deleted: 's

Formatted: Indent: First line: 0.5"

Deleted: the

Deleted: Liu (2008b)

Deleted: relation

Deleted: three

Deleted: car

Deleted: sky

Deleted: ,

Deleted: , and upward emission from the surface and the atmosphere below cloud but being scattered back by the cloud...

265
$$\text{LWP} = \frac{\lambda \rho_L}{6\pi \Im \left\{ \frac{m^2 - 1}{m^2 + 2} \right\}} \ln(1 - \epsilon_c), \quad (4)$$

266 where m is the refractive index of water at temperature T_c , λ is wavelength, ρ_L is liquid
 267 water density (1000 kg m^{-3}) and $\Im\{\}$ indicates taking the imaginary part. In this study, the
 268 refractive index of liquid water is calculated based on Liebe et al. (1993). It should be
 269 cautioned that the refractive index at high microwave frequencies may not be very accurate
 270 for supercooled liquid water as pointed by Kneifel et al. (2014), which can result in errors
 271 in the liquid water path estimation. Another error in the liquid water path estimation can
 272 be caused by the omission of the reflection by snow particles to the upwelling radiation
 273 originated from surface emission in the retrieval algorithm. Based on estimation by Kneifel
 274 et al. (2010), this reflection can enhance downward radiation by 5 K at 89 GHz where
 275 heavy snow cloud occurs. The formulation of the current liquid water path retrieval
 276 algorithm has the advantage of using cloud-free observations (T_{Ba} in Eq.3) as background
 277 to calculate cloud emissivity, which is particularly useful when water vapor observations
 278 are lacking. However, the drawback is that it cannot include the contribution by ice
 279 scattering.

Formatted: Subscript

280 In Fig. 1 shown is an example of the liquid water path retrieved in this study together
 281 with radar reflectivity cross sections and liquid water path retrieval from the manufacture-
 282 provided algorithm. It is seen that in cloud-free regions our liquid water path retrievals are
 283 close to zero, while the manufacture-provided retrievals have a positive bias of about 30 g
 284 m^{-2} . In cloudy regions, the two liquid water path values compare much closer to each other.
 285 Based on this comparison, we believe that the liquid water path values retrieved in this
 286 study are more reasonable. Therefore, our retrievals will be used in the following analysis.

Deleted: clear-sky

287 **2.3 Snowing Cloud Detection**

288 All snow events have been identified from the RPG-FMCW observations during 1
 289 November 2017 through 30 April 2018 (6 months). To separate snow and rain at surface,
 290 the scheme of Sims and Liu (2015) is implemented. In their study, the effects of multiple
 291 geophysical parameters on precipitation phase were investigated using global surface-
 292 based observations over multiple years. They showed that wet-bulb temperature is a key
 293 parameter for separating solid and liquid precipitation and the low-level temperature lapse

Deleted: ground

296 rate also affects the precipitation phase. Geophysical parameters from MERRA-2
297 reanalysis (Gelaro et al., 2017) were used in this study as input to the Sims and Liu (2015)
298 scheme. In addition, we use the near-surface reflectivity higher than -20 dBZ as the
299 criterion for snowfall detection; all radar data analyzed for snowing clouds in the following
300 sections have a near-surface radar reflectivity greater than -20 dBZ. In a study by Wang et
301 al. (2017) based on CloudSat radar reflectivity profiles, they found that precipitation onset
302 often occurs when radar reflectivity is about -18 to -13 dBZ. We use the value of -20 dBZ
303 as criterion in this study to make sure that all possible snowfall cases are included in the
304 precipitation samples.

Deleted: the Modern Era Reanalysis for Research and Applications Version-2 (

Deleted:)

Deleted: a

305 Cloud top height is used for the determination of cloud types. As shown in Fig.2,
306 radar reflectivity above cloud top is often noisy as shown between 11 and 16 UTC.
307 Therefore, it is often problematic to determine cloud top height by simply using a radar
308 reflectivity threshold. However, we found that Doppler spectral width is a reliable indicator
309 to identify clouds as shown in the bottom panel in Fig.2. Using visual examination of this
310 and some other cases, we found that Doppler spectral width commonly reduces to less than
311 0.1 m s^{-1} above cloud top. In Fig. 2, we show in the upper panel the cloud top height in the
312 black solid line as determined by the criterion of the spectral width $>0.1 \text{ m s}^{-1}$ for snowing
313 clouds with near-surface radar reflectivity greater than -20 dBZ . It appears that the
314 criterion well captures the cloud tops.

Deleted: criteri

Deleted: a

Deleted: criteria

315 2.4 Other Ancillary Data

316 While quantitative analysis was not conducted, data collected at the same location by
317 PARTicle SIZE VELOCITY (PARSIVEL; Löffler-Mang and Joss, 2000; Battaglia et al., 2010;
318 Tokay et al., 2014), 2-Dimensional Video Distrometer (2DVD; Kruger and Krajewski,
319 2002), and Multi-Angle Snowflake Camera (MASC; Garrett et al., 2012; Grazioli et al.,
320 2017) are used for confirmation of precipitation phase and particle types. A PARSIVEL is
321 an optical disdrometer which uses a 54 cm^2 laser beam in the wavelength of 650 nm. It
322 measures the size and fall velocity of individual precipitation particles with diameter
323 ranging from 0.2 mm to 25 mm for solid particles. An autonomous PARSIVEL unit (Chen
324 et al., 2017) from NASA was collocated with the RPG-FMCW cloud radar during the field
325 campaign. A collocated 2DVD provides detailed information on size, fall velocity, and

333 shape of individual hydrometeors with two orthogonal fast line-scan cameras. The camera
334 provides images of particles which are matched for individual particles. The matched
335 individual particles are then corrected for shape distortion. In addition, detail images of
336 particles are provided from MASC that is composed of three cameras separated
337 horizontally by an angle of 36 degrees and simultaneously takes high-resolution (35 μm
338 per pixel) photographs of free-falling hydrometeors. Hydrometeor classification algorithm
339 based on the supervised machine learning technique (Praz et al., 2017) is applied to the
340 individual images of particles. This procedure identified the precipitation type (small
341 particles, columnar crystals, planer crystals, combination of columnar and plate crystals,
342 aggregates, and graupel) and the degree of riming.

343 2.5 Dividing Snowing Clouds to Three Types

344 There are several synoptic weather patterns that cause snowfall over the Pyeongchang
345 area. The first pattern is a synoptic low pressure system, so-called “cold low”, developed
346 over the Yellow sea (west of Korea) or cold continent and causes the snowfall over the
347 northern or middle part of Korea when moving to east (Chung et al. 2006; Ko et al. 2016;
348 Park et al. 2019). As this system crosses the Korean peninsula, the system become weaker
349 and shallower once moving over the Pyeongchang area. The precipitation intensity and
350 depth of system depend on the strength of low pressure. The second synoptic pattern,
351 “warm low,” develops over the warm ocean near East China sea or South sea and moves
352 to north-east or east (Nam et al. 2014; Gehring et al 2020). This synoptic pattern brings
353 abundant moisture to Korean Peninsula and is typically favored for vertically well-
354 developed precipitation system. As the warm low pressure passes the Korean Peninsula
355 and East sea, the winds over the Pyeongchang area and East sea turns to easterly or north-
356 easterly, bringing in cold air to the east coastal area. Thus, we expect that the depth of
357 precipitation system is likely first deep with large moisture and later becomes shallower as
358 influenced by north-easterly cold air. The third interesting pattern, so-called “air-sea
359 interaction”, is developed by the easterly or north-easterly flow due to the Kaema high over
360 the northern mountain complex or high pressure over Manchuria by the eastward expansion
361 of the Siberian high (Kim and Jin 2016; Kim et al 2019). Thus, the cold north-easterly or
362 easterly flow enhances the interaction with warm moisture ocean, resulting in the
363 development of shallow convection and thermal inversion in the lower troposphere. The

Deleted: 2.5

Formatted: Font: (Default) Times New Roman, 12 pt

Formatted: List Paragraph, Outline numbered +
Level: 2 + Numbering Style: 1, 2, 3, ... + Start at: 4 +
Alignment: Left + Aligned at: 0" + Indent at: 0.25"

Formatted: Indent: First line: 0.25", Line spacing: 1.5
lines

365 shallow convective clouds move to the coastal and mountain area where they are lifted by
366 the orography.

367 An example of radar reflectivity cross section is shown in Fig.1 where deeper clouds
368 lead to shallower convective cells. This is the case of the second synoptic type, warm low.
369 During the passage of the warm low, the system reached to 9 km. However, the
370 precipitation system is shallower than 1 km during easterly or north-easterly flow when the
371 warm low pressure passed the East sea. In consideration of the implications to satellite
372 snowfall remote sensing, we group the snowing clouds into three types: deep, shallow and
373 near-surface. The “deep” snowing clouds are those with cloud top higher than 4 km, which
374 are considered to be easily detected by both space-borne radars and radiometers at high
375 microwave frequencies. They are mostly generated by large-scale lifting of frontal systems.
376 We define the “shallow” snowing clouds as those with cloud top between 1.5 and 4 km.
377 Large part of the snowing clouds in this group are associated with convective cells in
378 unstable airmasses after the passing of fronts. These are the group that space-radars and
379 radiometers may sometimes have difficulties to detect because of their shallowness and
380 liquid-water rich. The “near-surface” group is defined as those having cloud top lower than
381 1.5 km. Similar to the case of shallow snow clouds, the near-surface snow clouds also
382 mostly occur after low pressure passing or during north-easterly/easterly flow, and are
383 convective in nature. Because of their shallowness, this group of snowing clouds will likely
384 be hidden within ground-clutters for space-radars. Ground-based observations have the
385 advantage to detect them from bottom up.

386 In Fig. 1, examples are shown for the three snowing cloud types, together with liquid
387 water path retrieved from RPG-FMCW observations using algorithms described in section
388 2.2. In this case, the largest value of liquid water path was seen in the transition from
389 shallow to near-surface snowing clouds near 12 UTC, while the strongest radar reflectivity
390 values (i.e., the heaviest snowfall) occurred in the deep snowing cloud between 01 to 05
391 UTC on 24 December 2017.

392 Surveying all observed data for the entire winter, approximately 374 hours of
393 observations are deemed as snowfall events after we apply the -20 dBZ threshold at the
394 lowest bin and the Sims and Liu (2015) algorithm to exclude rain events. These

Deleted: ¶

Formatted: Font: (Default) Times New Roman, 12 pt

Deleted: The winter weather at the observational site is largely influenced by passing storms associated with low-pressure frontal systems. A common radar reflectivity cross section is similar to that shown in Fig.1 where deeper clouds lead to shallower convective cells. The deeper clouds are related to the low-pressure system crossing the Korean peninsula or passing its south and the shallower clouds are linked to air-sea interaction under the control of a high-pressure cold air system after front passing.

Formatted: Font color: Auto

405 observations are then averaged over each 5-minute interval to form 4491 samples. The
406 relative frequencies of occurrence (area fraction, calculated by the number of samples of a
407 given snow type divided by the total number of snowfall samples) and snowfall amount
408 (volume fraction, calculated by the snowfall amount produced by a given snow type
409 divided by the total snowfall amount by all types) for the three types of snowing clouds are
410 shown in Fig.3. The snowfall volume is the accumulated snowfall with the rate estimated
411 by Eq.(2) from radar reflectivity at the lowest bin. Over half (67.4%) of the observed
412 samples are near-surface snowfall, followed by shallow (21.2%) and then deep (11.4%)
413 snowing clouds. However, deep snowing clouds contribute the most to the total snowfall
414 volume (45.3%), followed by shallow (28.5%) and then near-surface (26.2%) snowing
415 clouds. Pettersen et al. (2020) analyzed snowing clouds observed by a micro rain radar at
416 Marquette, Michigan for 4 winter seasons. Snow clouds are divided into shallow (top
417 height lower than 1.5 km) and deep events. They found that shallow clouds occur 2 times
418 as often as deep clouds while both types contribute almost equally to annual snowfall
419 accumulation. Those statistics are very similar to the results obtained in this study for
420 snowfall events observed at Pyeongchang, Korea. Kulie et al. (2016) found that globally
421 shallow snow clouds can be associated with strong convections and heavy snowfall. The
422 snowfall rates for shallow and near-surface snow clouds observed in this study are mostly
423 lower than 0.5 mm h^{-1} ; heavy snowfall is mainly associated with deep snow clouds. One
424 possible explanation of the difference is as follows. The snowfall from shallow and near-
425 surface snow clouds in this study mostly comes from convections associated with cold
426 airmass outbreak from the northwest. Since the observation site is in the mountains in the
427 east coastal region of the Korean Peninsula, substantial portion of the moisture picked up
428 by the cold air from the warm ocean in the Yellow Sea (west of the Korean Peninsula) has
429 been already transformed to snow before reaching the observation site. In addition, the
430 convective clouds and easterly flow can cross the mountains and produce heavy snowfall
431 over the site in the case of strong winds and lower thermal stability. However, these types
432 of events occurred relatively infrequently during the experiment when compared to the
433 other snowfall types. Consequently, the snowfall associated with shallow and near-surface
434 clouds at this site is relatively moderate.

Deleted: t

Deleted: As described earlier, we used -20 dBZ at the lowest bin to identify snow events.

Deleted: e

Formatted: Superscript

Formatted: Font color: Auto

Deleted: were

Deleted: relatively

Deleted: less

Deleted: with

Deleted: average

Deleted: events

Deleted:

447 3. Microphysical Properties of Snowing Clouds

448

449 3.1 Case Examples

450 (a) Deep and “dry” followed by near-surface snowing clouds

451 From 7 to 8 March 2018, a low-pressure system passed the south of the Korea
452 Peninsula, and solid precipitation was observed at the radar site from 09 UTC on the 7th
453 through 24 UTC on the 8th. In Fig.4 shown are cross section of radar reflectivity and time
454 variation of liquid water path and snow water path (SWP, vertically integrated snow water
455 content). Surface PARSIVEL and 2DVD observations indicated that snow particle types
456 are mostly snowflakes from 09 UTC on the 7th to 06 UTC on the 8th, while rimed ice
457 particles and graupels are also observed then after. The radar and radiometer observations
458 indicate that the deep clouds have cloud top higher than 8 km and peak snow water path
459 value about 500 g m⁻². However, liquid water in the deep clouds is low, with liquid water
460 path constantly below 150 g m⁻². Once the deep clouds pass the station, the clouds became
461 much shallower, mostly being classified as near-surface snowing clouds. However, their
462 liquid water path increased substantially with peak values close to 600 g m⁻², which is
463 consistent with the observed rimed ice particles and graupels during this period.

464 (b) Deep and “wet” followed by shallow snowing clouds

465 On 28 February 2018, deep snowing clouds associated with a low-pressure system
466 were observed at the radar site, followed by shallow snowing clouds that lasted till 03 UTC
467 on March 1. Radar reflectivity, liquid water path and snow water path are shown in Fig.5.
468 Surface PARSIVEL observations indicated melting snow with surface air temperature near
469 0°C before 04 UTC on February 28, which may have contributed the liquid water path peak
470 around 04 UTC. Heavy snowfall was observed from 04 to 14 UTC on 28 February;
471 snowflakes observed at surface are large aggregates and show indications of riming
472 occurred. Liquid water path was high for both the deep and shallow clouds with peaks
473 higher than 400 g m⁻² even without including the portion of melting snow before 04 UTC
474 on the 28th. Rimed snow particles were observed at surface corresponding to the shallow
475 snow cell based on 2DVD and MASC data.

476 3.2 Liquid versus Ice in Snowing Clouds

Deleted: 400

478 During the 6-month period, a total of 374 hours of snow precipitation have been
479 observed by the RPG-FMCW. The frequency distributions of 5-minute averaged surface
480 snowfall rate and liquid water path are shown in Fig.6 with both surface snowfall rate and
481 liquid water path in logarithm scale. On average, deeper clouds generate heavier snowfall;
482 near-surface and shallow snowing clouds produce snowfall rarely heavier than 0.5 mm h^{-1} ;
483 while snowfall rate in deep snowing clouds reaches over 1 mm h^{-1} . Higher values of
484 cloud liquid water path are also more likely observed in deeper clouds. However, the
485 likelihood of a substantial amount of liquid water in shallower clouds is also high. For
486 example, for the liquid water path range of $100\sim 250 \text{ g m}^{-2}$ the frequency values are still
487 reaching about 10% for near-surface and shallow snowing clouds. On the upper limit,
488 liquid water path in all clouds only occasionally exceeds 500 g m^{-2} .

489 In Fig.7, we show the scatterplot of surface snowfall rate versus liquid water path
490 averaged over a 5-minute period. As indicated in case studies earlier, the two variables
491 hardly vary in a correlated fashion, neither positively nor negatively. For deep snowing
492 clouds, the heaviest snowfall corresponds to a liquid water path of about 200 g m^{-2} , while
493 further increasing in liquid water path does not seem to enhance surface snowfall. For
494 shallow and near-surface snowing clouds, the snowfall rate is confined between 0 to 0.6
495 mm h^{-1} while liquid water path stretches from 0 to 600 g m^{-2} without coherent variation
496 between liquid water path and surface snowfall rate. Additionally, unlike heavy snowfall
497 preferably occurring in deep snowing clouds, large values of liquid water path (say > 300
498 g m^{-2}) are almost equally probable to be found in near-surface, shallow and in deep snowing
499 clouds.

500 The mean state and its variability of cloud liquid water are also examined in the 2-
501 dimensional space of near surface radar reflectivity and cloud top height, as shown in Fig.8.
502 In this figure, the mean values of (a) the number of occurrences, (b) liquid water path, and
503 (c) standard deviation of liquid water path in each 2 dBZ by 500 m grid are shown based
504 on the 5-minute averaged data. The number of occurrences diagram indicates that heavier
505 snowfall (stronger radar reflectivity) tends to have a higher cloud top for cases with near
506 surface radar reflectivity greater than 0 dBZ although this tendency is not clear for cases
507 with lower values of near surface radar reflectivity. [The diagrams for mean and standard](#)

508 deviation of liquid water path shown in Figs.8b and 8c appear to indicate the following.
 509 For deep snow clouds (top higher than 4 km) with surface radar reflectivity greater than 6
 510 dBZ, liquid water path has a large mean value but a small standard deviation. On the other
 511 hand, shallow snow clouds (top between 1.5 and 4 km) with moderate surface radar
 512 reflectivity (0-5 dBZ) have a moderate mean value but a high variability of liquid water
 513 path. There is an area with high mean value and high variability of liquid water path located
 514 at surface radar reflectivity between -10 and 0 dBZ and cloud top height between 4 and 6
 515 km, possibly corresponding to convective cells in early developing stage. For near-surface
 516 and shallow clouds, both the mean value and standard deviation of liquid water path appear
 517 to increase as surface radar reflectivity increases.

518 To express the “dryness” of the snowing clouds, one may use the glaciation ratio
 519 (GR) defined as (Liu and Takeda, 1988):

$$520 \quad GR = \frac{SWP}{LWP+SWP} \times 100\% . \quad (5)$$

521 The GR parameter indicates the fraction of total condensed water in the column that has
 522 been converted to solid phase. In Fig.9, we show how the GR values are related to (a) cloud
 523 top height, (b) surface snowfall rate and (c) cloud mean temperature (temperature at the
 524 geometrical middle of a reflectivity profile). Generally speaking, clouds with higher tops,
 525 associated with higher snowfall rate or with colder mean temperature tend to have higher
 526 degrees of glaciation, although the scatters are extremely large. For example, for a shallow
 527 snowing cloud with 0.2 mm h⁻¹ snowfall rate, its glaciation ratio can be any value from
 528 near 0 to about 100%, probably depending on the development stage of individual cells. In
 529 Fig.9a, there is a concentration of points with high cloud top (>5 km) but glaciation ratio
 530 between 50% and 75% rather than 100%. It is likely that the phenomena are caused by
 531 clouds that have multiple layers or a cloud layer with dynamically decoupled upper and
 532 lower portions. Corresponding to the clouds with their heaviest snowfall rate, deep snowing
 533 clouds have a glaciation ratio of about 60% while shallow and near-surface snowing clouds
 534 only have their glaciation ratio less than 20%, which adds extra difficulties for detecting
 535 snow in these types of clouds by passive microwave observations. There is loosely a trend
 536 that clouds with a lower mean temperature have a higher degree of glaciation. For near-

Deleted: On average, the higher values of liquid water path are along the right-most edge of the data-covered area in the plot, indicating that given the same surface snowfall rate clouds with the lowest top height tend to contain the highest amount of liquid water. The variability of liquid water path as expressed by its standard deviation further indicates that liquid water path in clouds with lower top heights is more variable in magnitude as well.

545 surface snowing clouds, this trend is less clear with their glaciation degree hardly over 50%.
546 Using data observed over Greenland, Pettersen et al. (2018) found that snowfall events for
547 frontal deep clouds are often ice clouds with little liquid water while shallower clouds are
548 typically mixed-phase clouds and contain plenty of supercooled liquid water. Their low
549 glaciation rate for shallower clouds is similar to the result of this study.

550 3.3 Vertical Structures

551 The mean vertical structure of the snowing clouds may be expressed by contoured
552 frequency by altitude diagrams (CFADs; Yuter and Houze, 1995) of radar reflectivity,
553 mean Doppler velocity, and Doppler spectral width, as shown in Fig. 10. For deep snowing
554 clouds, the radar reflectivity CFADs show a relatively narrow spread with a sharp radar
555 reflectivity decreases with the increase of altitude above 4 km (“left-tilting” structure),
556 implying that most of the precipitation growth occurs above 4 km. For shallow clouds, the
557 “left-tilting” structure starts from near surface and the frequency has broader distribution
558 at each level. In contrast, the near-surface snowing clouds do not show such “left-tilting”
559 structure, but rather have a broad distribution below their cloud top height, indicating that
560 the precipitation maximum does not necessarily situate near the surface in these profiles.
561 We interpret that the broad distribution of frequencies at each level is likely due to the
562 convective nature of these clouds, so that the precipitation profile is largely determined by
563 the development stage of the clouds. For example, developing clouds have their
564 precipitation maximum in the upper portion while matured clouds have their precipitation
565 maximum in the lower portion in the vertical profiles.

566 For mean Doppler velocity, the most likely values are around -1 m s^{-1} (the negative
567 sign indicates downward movement), corresponding to the terminal velocity of unrimed to
568 moderately rimed aggregates (Locatelli and Hobbs, 1974). There is a tendency that
569 particles in upper levels fall somewhat slower than those in the lower levels. The Doppler
570 spectral width indicates that particles in the upper levels have a narrower spectrum.
571 Combining the vertical profiles of mean Doppler velocity and spectral width, it is
572 concluded that ice particles at upper levels have a narrower size distribution and lower
573 terminal velocity. It is also interesting to notice that there seems to be a regime shift for
574 deep snow clouds near 4 km altitude; the frequency patterns appear to be different below

Deleted: (a)

Deleted: (b)

Deleted: (c)

Deleted: 3

Deleted: 3

580 and above this level for all the CFADs of radar reflectivity, Doppler velocity and spectrum
581 width. Additionally, the slope of reflectivity suddenly changes around 8 km and the
582 absolute value of Doppler velocity reduced dramatically below 8 km. A similar feature
583 also appeared in the long-term observation with cloud radar (see Figs. 16 and 17 of Ye et
584 al. 2020). The shift of growth regime was appeared at 8 km height (3~3.5 km above the
585 bright band peak and corresponding to $\sim -17^{\circ}\text{C}$). This regime shift induced the updraft
586 (reached 1 m s^{-1}) below this layer. However, Ye et al. (2020) could not explain the linkage
587 between this regime shift and updraft below. ~~While it is beyond the scope of this study,~~
588 ~~this phenomenon will be an interesting topic for future research on the cloud~~ microphysics
589 ~~in this region.~~

Deleted: T

Formatted: Font color: Auto

Deleted:

Deleted:

Deleted:

Deleted: The shifts are consistent to the assumption that the main precipitation growth region is located above 4 km.

Deleted: dynamics

590

591 4. Implications to Passive Microwave Remote Sensing

592

593 To understand how the microphysical properties in snowing clouds impact on
594 passive microwave remote sensing, a radiative transfer model simulation at GPM/GMI
595 channels has been conducted using the measured liquid and snow water quantities as a
596 guidance for the model input. The radiative transfer model developed by Liu (1998) has
597 been used in this simulation, which uses a four-stream discrete ordinates method to solve
598 the radiative transfer equation. For snow particles, the single-scattering properties
599 calculated by discrete dipole approximation for sector type snowflakes (Liu, 2008b) are
600 used. Based on studies of Geer and Baordo (2014), the single-scattering properties for the
601 sector type snowflakes work reasonably well in radiative transfer simulations for middle
602 latitude snowstorms. Since the emphasis of this study is to assess the impact of cloud
603 microphysics on satellite remote sensing, the variability of surface emissivity is not
604 considered. In all the following simulations, we assign an emissivity of 0.9 for land surface
605 for all GMI channels and a 5 m s^{-1} wind speed over ocean to compute surface emissivity.

606 4.1 Masking Effect to Scattering Signatures by Cloud Liquid Water

614 Based on analysis shown in section 3.2, liquid water path frequently varies from 0
615 to 500 g m⁻² for any of the 3 types of snowing clouds while snowfall rate at surface
616 commonly reaches to 0.3, 0.5, and 1.0 mm h⁻¹, respectively, for near-surface, shallow, and
617 deep clouds. We examine how the cloud liquid would mask the ice scattering at two GMI
618 frequencies, 89 and 166 GHz, at viewing angles of 53° for 89 GHz and 49° for 166 GHz
619 using radiative transfer calculations. Using clear-sky brightness temperature T_{B0} as the base,
620 Figure 11 shows how brightness temperature varies as liquid water path and surface
621 snowfall rate increase. Note that in these radiative transfer calculations, mean snowfall rate
622 profiles derived from observations are used. The mean profiles are derived as follows. We
623 first group all the observed snowfall rate profiles according to their cloud type, and then
624 for each cloud type we average those profiles that fall into a given snowfall rate bin. A 1-
625 km deep liquid cloud layer is placed at 0.5-1.5 km, 2.5-3.5 km and 4.5-5.5 km, respectively,
626 for near-surface, shallow, and deep clouds. The liquid water path is increased from 0 to
627 500 g m⁻².

Deleted: w

Deleted: used

Deleted: derived for each

Deleted: d

Deleted: for various

Deleted: s

628 For near-surface snowing clouds, the decrease of brightness temperature due to ice
629 scattering is very limited for either 89 or 166 GHz, only about 1.5 K for 89 GHz and 2.5 K
630 for 166 GHz, occurring when liquid water path is very low. Therefore, most likely this type
631 of clouds displays a warming signature in the passive microwave observations due to the
632 existence of liquid water clouds. For shallow snowing clouds, the modeling results show
633 there is still a mostly warming at 89 GHz and an equal mix of warming and cooling at 166
634 GHz. The masking effect still remains quite significant at 89 GHz even for deep snowing
635 clouds; it can cause an increase in brightness temperature by more than 5 K from clear-sky
636 value. The dominant scattering signature shows at 166 GHz for deep clouds. At surface
637 snowfall rate of 1 mm h⁻¹, brightness temperature can decrease from clear-sky value by
638 more than 30 K (color bar only shows up to -15 K) when liquid water path is lower than
639 100 g m⁻².

Deleted: a few

Deleted: Kelvin

640 Based on the above modeling results, it is clear that if only relying on scattering
641 signature, i.e., brightness temperature depression, an algorithm will totally fail in retrieving
642 snowfall rate for near-surface clouds and partially fail for shallow clouds. Even for deep
643 snowing clouds, cloud liquid water will impact snowfall retrieval with a result of an

652 ~~overestimation for low and an underestimation for high values of liquid water path,~~
653 Therefore, a more plausible approach to the retrieval problem is to use a statistical method
654 in which the algorithm utilizes any regularities naturally existing between cloud liquid and
655 snow profiles to search for the most likely snowfall rate. One such approach is the Bayesian
656 retrieval algorithm (Kummerow et al., 1996; Olson et al., 1996; Seo and Liu, 2005). This
657 approach requires that the *a priori* database used in the retrieval has the same characteristics
658 in both microphysical properties and occurring frequency as those in natural clouds.

Deleted: The only cloud type that may have reliable retrievals is the deep snowing cloud.

659 4.2 A Bayesian Retrieval Exercise

660 In this section, an idealized experiment is designed to examine how a Bayesian
661 retrieval algorithm would perform for the three types of snowing clouds if we only take
662 into account the error caused by the variability of liquid water path and snowfall rate
663 profiles. In other words, we examine how well a Bayesian retrieval algorithm would
664 perform, when assuming no variations in surface emissivity, snowflakes being a fixed type,
665 and particle size distribution following an exponential form. Therefore, this exercise
666 mainly assesses the problems caused by the uncertainties associated with cloud liquid and
667 snow amounts.

668 First, a total of ~~30870~~ 5-minute averaged snow profiles are constructed from the 6
669 months long surface radar observations (including zero snowfall profiles). Each of the
670 snow profile is accompanied with a liquid water path which is assigned to be a 1 km deep
671 layer at 0.5-1.5 km, 2.5-3.5 km and 4.5-5.5 km, respectively, for near-surface, shallow, and
672 deep clouds. Atmospheric temperature, pressure, and relative humidity profiles are also
673 assigned to these profiles by interpolating MERRA-2 data spatially and temporally to the
674 individual snow profiles. A radiative transfer model calculation is then performed to
675 generate brightness temperatures at 11 GMI channels (all except the 10.7 GHz GMI
676 channels) using the above profiles as input. The 10.7 GHz channel is not considered here
677 because its brightness temperature is ~~not sensitive~~ to either liquid or ice hydrometeors and
678 its GMI channel has too large a footprint size compared to other channels. It is also assumed
679 that surface skin temperature is the same as surface air temperature and surface emissivity
680 is a constant (0.9 for land) for all channels. A sector type snowflake (Liu, 2008b) and an
681 exponential particle size distribution (Sekhon and Srivastava, 1971) are used for all the

Deleted: 18752

Deleted: merely sensible

686 cases. We then randomly divided the 30870 profiles and their computed brightness
687 temperatures into two equal-number groups; one is used as the *a priori* database for the
688 Bayesian retrieval algorithm, and the other as “observations” to test how well the surface
689 snowfall rate can be retrieved from the “measured” brightness temperatures. To mimic a
690 possible random error in the measured brightness temperatures, a random noise with a
691 maximum magnitude of 1 K is added to the “measured” brightness temperatures before
692 retrieval is performed. A detailed description of the Bayesian retrieval method can be found
693 in Seo and Liu (2005).

Deleted: 18752

694 In Fig.12 shown are the scatterplots of “measured” versus retrieved surface
695 snowfall rate, separated by snow cloud types. The correction as indicated by R^2 (square of
696 linear correlation coefficient), bias and root-mean-square (rms) difference are shown in
697 each diagram. The biases between the “measured” and retrieved snowfall rate are small for
698 all snow cloud types, with values of 0.019, 0.033, and 0.03 mm h⁻¹ for near-surface, shallow
699 and deep snowing clouds, respectively. The values of rms differences are also small; they
700 are 0.05, 0.11, and 0.16 mm h⁻¹, respectively, for near-surface, shallow and deep snowing
701 clouds. The color of the points in the figures indicates the value of liquid water path
702 associated with individual profiles. Clearly, as the cloud layer deepens, the skill of the
703 retrieval improves. The values of R^2 increases from 0.32 for near-surface clouds, to 0.41
704 for shallow clouds, and to 0.62 for deep clouds. That is, the retrievals can resolve 32%,
705 41%, and 62% of the variances in snowfall rate observations for near-surface, shallow and
706 deep clouds, respectively.

Deleted: is

Deleted: There is virtually no bias

Deleted: values

Formatted: Superscript

Formatted: Superscript

Deleted: 3

Deleted: 8

Deleted: 74

Deleted: one-third, one-half and three-fourths

Deleted: Another observation from the plots is that departure of points from the one-to-one line does not seem to relate to the magnitude of liquid water path, which implies that it is the randomness in the combination of liquid water path and snowfall rate that is reducing the algorithm’s skill, rather than the magnitude of liquid water path itself.

707 A question one may naturally want to ask is: Will the retrieval skill be improved if
708 the same clouds were moved to areas over ocean where liquid water information is
709 distinguishable at some microwave channels (e.g., 89 GHz)? To answer this question, we
710 perform the same retrieval exercise as mentioned above but assuming the clouds are over
711 an ocean surface with a constant surface wind speed of 5 m s⁻¹. Similarly, half of the 30870
712 samples are used as a priori database and half as “observations”. The retrieval results are
713 shown in Fig.13. Similar to land cases, the biases and rms differences have small values
714 for all cloud types. For deep snowing clouds, the R^2 statistic indicates only small
715 improvement in retrieval skills between over land and over ocean cases, although a visual

Deleted: 18752

Deleted: virtually no difference

732 inspection of the scatterplot shows that a better correspondence between “measured” and
733 retrieved values at snowfall rates lower than 0.2 mm h⁻¹. The improvement in retrieval
734 skills for over ocean shallow clouds is moderate with R² of 0.54 versus 0.41 over land. The
735 most significant improvement in retrieval skills occurs for over ocean near-surface snowing
736 clouds, in which R² increases from 0.32 over land to 0.52 over ocean. Note that land surface
737 emissivity and ocean surface wind are fixed in the retrieval exercises. Therefore, the
738 improvement is not due to a better knowledge of surface conditions, but rather due to the
739 richer information content on cloud microphysics contained in “measured” brightness
740 temperatures over ocean. One such piece of information must have come from the
741 brightness temperature difference between two polarizations over ocean, which remains
742 mostly zero over land surfaces. The results shown in Fig.13 indicate that the extra
743 polarization information helps the most for retrieving snowfall in shallower clouds.

744 In Figs. 12 and 13, it is also noted that an underestimation occurs when snowfall
745 rate is greater than 0.7 mm h⁻¹ for deep snowing clouds regardless over land or ocean. This
746 underestimation may be due to the deficiency of the Bayesian scheme, in which the
747 retrieval is a weighted average of snowfall rates of datum points in the a priori database
748 that are radiometrically consistent with observations. When an observation is close to the
749 upper boundary (i.e., high snowfall rates) in the database, the averaging takes more number
750 of datum points with snowfall rates lower than the actual value than those with higher
751 snowfall rates (no more datum points beyond upper boundary), thus resulting in an
752 underestimation.

753 To understand the information conveyed in polarization difference of brightness
754 temperatures, we performed a similar simulation to that described in Section 4.1, but
755 replaced land surface to ocean surface with a wind speed of 5 m s⁻¹. The changes of
756 depolarization as liquid water path and snowfall rate increase are shown in Fig.14 for each
757 of the 3 cloud types at 89 and 166 GHz. Depolarization is defined as $\Delta T_B = T_{BV} - T_{BH}$, where
758 T_{BV} and T_{BH} are brightness temperatures at vertical and horizontal polarizations,
759 respectively. The change is relative to clear-sky values, ΔT_{B0} . The change in depolarization
760 at 89 GHz is well corresponding to the change in liquid water path, without much
761 dependence on snowfall rate, particularly for near-surface and shallow snowing clouds.

Deleted: marginal

Deleted: 54

Deleted: 48

Deleted: 33

Deleted: 54

Deleted: near-surface

Formatted: Superscript

768 Therefore, it is plausible that the increased retrieval skill over ocean for near-surface and
769 shallow clouds is due to the added information on liquid water contained in the polarization
770 differences. Comparing Figs.12 and 13, it seems that the added information is particularly
771 helpful in improving retrievals at low snowfall rates.

772

773 5. Conclusions

774

775 During the 2017-18 winter season, a ground-based radar and radiometer
776 observation has been carried out over Korean Peninsula as part of the ICE-POP 2018
777 campaign. Using the coincident radar and radiometer data, we were able to retrieve cloud
778 liquid water path, snow water content and snowfall rate. These microphysical properties
779 and their relation to cloud top height are analyzed in an effort to better understand their
780 implications to satellite remote sensing of snowfall. In the analysis, we divide the
781 approximately 374 hours of observed snowing clouds into near-surface, shallow and deep
782 types, for which the cloud top height is below 1.5 km, between 1.5 and 4 km and above 4
783 km, respectively. The near-surface snowing clouds are most likely to be missed by
784 currently available space-borne radars because of the blind zone caused by the
785 contamination of surface clutter, and their shallowness and liquid water abundance may
786 also present challenges to satellite radiometer observations. In this region during the
787 observation period, the shallow snowing clouds commonly occur in unstable air mass after
788 the passing of a cold front. It can be detected by space-borne radars with sufficient low
789 minimum detectable radar reflectivity, but the mixture of cloud liquid emission and ice
790 scattering complicates the retrievals by passive microwave observations. The deep
791 snowing clouds are mostly located near frontal zones and low-pressure centers; their strong
792 ice scattering signature makes it the most favorable type among the three for snowfall
793 retrievals by both satellite radars and radiometers. Surveying all the observed data, it is
794 found that near-surface snowing cloud is the most frequently observed cloud type with a
795 frequency of occurrence over 60%, while deep snowing cloud contributes the most in
796 snowfall volume with about 50% of the total snowfall amount.

Deleted: T

798 The probability distributions of surface snowfall rates are clearly different among
799 the three types of snowing clouds, with vast majority of ~~them~~, hardly reaching to 0.3 mm h⁻¹
800 ¹ for near-surface, 0.5 mm h⁻¹ for shallow, and 1 mm h⁻¹ for deep snowing clouds. However,
801 liquid water path in the three types of snowing clouds all has substantial likelihood to be
802 between 0 to 500 g m⁻², although deeper clouds are somewhat more likely with more liquid
803 water as well. There is no clear correlation, either positive or negative, between surface
804 snowfall rate and liquid water path. However, given the same surface snowfall rate, clouds
805 with lower cloud top height tend to have higher liquid water path. The glaciation ratio
806 defined by the ice fraction in the total condensed water in an atmospheric column is
807 estimated and found to be related to cloud top height, surface snowfall rate and cloud mean
808 temperature, although the relations are very scattered. A higher value of glaciation ratio is
809 generally corresponding to a higher cloud top, a higher surface snowfall rate and lower
810 cloud mean temperature.

Deleted: it

811 Moreover, we examined the ability of a Bayesian type algorithm to retrieve surface
812 snowfall rate for snow events similar to those observed in this study when using GPM/GMI
813 observations. First, using the approximately 30,000 observed snow cloud and precipitation-
814 free profiles, brightness temperatures at GPM/GMI channels are computed. Then, these
815 snowfall rate and associated brightness temperature pairs are randomly divided into two
816 groups. One group is used as “observations”, and the other is used as the *a priori* database
817 of the Bayesian algorithm. Under idealized scenario, i.e., without considering the
818 uncertainties caused by surface emissivity, ice particle size distribution and particle shape,
819 the examination results indicate that the correlation as expressed by R² between the
820 “retrieved” versus “measured” snowfall rates is about 0.32, 0.41 and 0.62, respectively, for
821 near-surface, shallow and deep snowing clouds over land surface. Since this is an extremely
822 idealized retrieval exercise only dealing with the complicated mixture of cloud liquid and
823 snow profiles, these numbers basically indicate the upper limits of how a retrieval
824 algorithm can perform for these snowing clouds. A hypothetical retrieval for the same
825 clouds but over ocean is also studied, and a major improvement in skill for near-surface
826 clouds is found with R² increased from 0.32 to 0.52, while improvement in skill is small
827 for deeper clouds. The improvement is interpreted as that some liquid water information is
828 resolved by the polarization difference contained in the over-ocean brightness temperatures.

Deleted: Using

Deleted: 19

Deleted: cloud

Deleted: ,

Deleted: ability of a Bayesian type algorithm to retrieve surface snowfall is examined using half the profiles as observations and half as

Deleted: 33

Deleted: 48

Deleted: 74

Deleted: The result also implies that it is the randomness in the combination of liquid water path and snowfall rate that is limiting the algorithm’s skill, rather than the magnitude of liquid water path itself.

Deleted: 33

Deleted: 54

Deleted: virtually no change

Deleted: found

Deleted: and only marginal improvement is found for shallow clouds...

Deleted: seen in near-surface clouds

851 This information helps the most for the otherwise information-poor observations for the
852 near-surface clouds.

853 By analyzing the radar and radiometer data from one-winter-long observations and
854 the results of a Bayesian retrieval dry run, this study gives a general picture of the
855 characteristics of the different types of snowing clouds and points out the fundamental
856 challenges in retrieving their snowfall rate from passive microwave observations. It is
857 hopeful that these results can help developers improve physical assumptions in future
858 algorithms as well as data users better interpret satellite retrieved snowfall products. Lastly,
859 it is worth mentioning that there are still many valuable datasets, such as particle shape and
860 size distribution information from PARSIVEL, 2DVD and MASC, which we didn't
861 analyzed quantitatively in this study. A thorough analysis of those datasets in conjunction
862 with the remote sensing data will undoubtedly improve future snowfall retrieval algorithm
863 development.

864

865

866 **Acknowledgements.** This research has been supported by NASA under grants
867 80NSSC19K0718 and NNX16AP27G. Participation of KK and GWL has been supported
868 by the Korea Meteorological Administration Research and Development Program under
869 Grant KMI2020-00910, and by the Korea Environmental Industry & Technology Institute
870 (KEITI) of the Korea Ministry of Environment (MOE) as “Advanced Water Management
871 Research Program” (79615). The authors are greatly appreciative to the participants of the
872 World Weather Research Programme Research Development Project and Forecast
873 Demonstration Project, International Collaborative Experiments for Pyeongchang 2018
874 Olympic and Paralympic winter games (ICE-POP 2018), hosted by the Korea
875 Meteorological Administration.

876

877

References

878 Battaglia, A., Rustemeier, E., Tokay, A., Blahak, U. and Simmer, C.: PARSIVEL snow
879 observations: A critical assessment, J. Atmos. Ocean. Technol.,

Deleted: 18-06810

881 doi:10.1175/2009JTECHA1332.1, 2010.

882 Bennartz, R. and Bauer, P.: Sensitivity of microwave radiances at 85-183 GHz to
883 precipitating ice particles, *Radio Sci.*, 38(4), n/a-n/a, doi:10.1029/2002rs002626, 2003.

884 Casella, D., Panegrossi, G., Sanò, P., Marra, A. C., Dietrich, S., Johnson, B. T. and Kulie,
885 M. S.: Evaluation of the GPM-DPR snowfall detection capability: Comparison with
886 CloudSat-CPR, *Atmos. Res.*, 197, 64–75, doi:10.1016/j.atmosres.2017.06.018, 2017.

887 Chen, H., Chandrasekar, V. and Bechini, R.: An improved dual-polarization radar rainfall
888 algorithm (DROPS2.0): Application in NASA IFloodS field campaign, *J.*
889 *Hydrometeorol.*, doi:10.1175/JHM-D-16-0124.1, 2017.

890 Chen, S., Hong, Y., Kulie, M., Behrangi, A., Stepanian, P. M., Cao, Q., You, Y., Zhang,
891 J., Hu, J. and Zhang, X.: Comparison of snowfall estimates from the NASA CloudSat
892 Cloud Profiling Radar and NOAA/NSSL Multi-Radar Multi-Sensor System, *J. Hydrol.*,
893 541, 862–872, doi:10.1016/j.jhydrol.2016.07.047, 2016.

894 [Chung, S.-H., Byun, K.-Y., Lee, T.-Y.: Classification of snowfalls over the Korean](#)
895 [peninsula based on developing mechanism. *Atmosphere*. 16, 33–48, 2006.](#)

896 Draine, B. T. and Flatau, P. J.: Discrete-Dipole Approximation For Scattering
897 Calculations, *J. Opt. Soc. Am. A*, 11(4), 1491, doi:10.1364/josaa.11.001491, 1994.

898 Garrett, T. J., Fallgatter, C., Shkurko, K. and Howlett, D.: Fall speed measurement and
899 high-resolution multi-angle photography of hydrometeors in free fall, *Atmos. Meas.*
900 *Tech.*, doi:10.5194/amt-5-2625-2012, 2012.

901 Geer, A. J. and Baordo, F.: Improved scattering radiative transfer for frozen
902 hydrometeors at microwave frequencies, *Atmos. Meas. Tech.*, doi:10.5194/amt-7-1839-
903 2014, 2014.

904 [Gehring, J., Oertel, A., Vignon, É., Jullien, N., Besic, N., and Berne, A.: Microphysics](#)
905 [and dynamics of snowfall associated with a warm conveyor belt over Korea. *Atmos.*](#)
906 [*Chem. Phys.*, 20, 7373–7392, <https://doi.org/10.5194/acp-20-7373-2020>, 2020.](#)

907 Gelaro, R., McCarty, W., Suárez, M. J., Todling, R., Molod, A., Takacs, L., Randles, C.

908 A., Darmenov, A., Bosilovich, M. G., Reichle, R., Wargan, K., Coy, L., Cullather, R.,
909 Draper, C., Akella, S., Buchard, V., Conaty, A., da Silva, A. M., Gu, W., Kim, G. K.,
910 Koster, R., Lucchesi, R., Merkova, D., Nielsen, J. E., Partyka, G., Pawson, S., Putman,
911 W., Rienecker, M., Schubert, S. D., Sienkiewicz, M. and Zhao, B.: The modern-era
912 retrospective analysis for research and applications, version 2 (MERRA-2), *J. Clim.*,
913 30(14), 5419–5454, doi:10.1175/JCLI-D-16-0758.1, 2017.

914 Gong, J. and Wu, D. L.: Microphysical properties of frozen particles inferred from Global
915 Precipitation Measurement (GPM) Microwave Imager (GMI) polarimetric measurements,
916 *Atmos. Chem. Phys.*, 17(4), 2741–2757, doi:10.5194/acp-17-2741-2017, 2017.

917 Grazioli, J., Genthon, C., Boudevillain, B., Duran-Alarcon, C., Del Guasta, M.,
918 Madeleine, J. B. and Berne, A.: Measurements of precipitation in Dumont d’Urville,
919 Adélie Land, East Antarctica, *Cryosphere*, doi:10.5194/tc-11-1797-2017, 2017.

920 Honeyager, R., Liu, G. and Nowell, H.: Voronoi diagram-based spheroid model for
921 microwave scattering of complex snow aggregates, *J. Quant. Spectrosc. Radiat. Transf.*,
922 170, 28–44, doi:10.1016/j.jqsrt.2015.10.025, 2016.

923 Hudak, D., Rodriguez, P. and Donaldson, N.: Validation of the CloudSat precipitation
924 occurrence algorithm using the Canadian C band radar network, *J. Geophys. Res.*, 113,
925 D00A07, doi:10.1029/2008JD009992, 2008.

926 Katsumata, M., Uyeda, H., Iwanami, K. and Liu, G.: The response of 36- and 89-GHz
927 microwave channels to convective snow clouds over ocean: Observation and modeling, *J.*
928 *Appl. Meteorol.*, 39(12 PART 2), 2322–2335, doi:10.1175/1520-
929 0450(2000)039<2322:troagm>2.0.co;2, 2000.

930 Kim, M. J., Weinman, J. A., Olson, W. S., Chang, D. E., Skofronick-Jackson, G. and
931 Wang, J. R.: A physical model to estimate snowfall over land using AMSU-B
932 observations, *J. Geophys. Res. Atmos.*, doi:10.1029/2007JD008589, 2008.

933 [Kim, J., Yoon, D., Cha, D. H., Choi, Y., Kim, J. and Son, S. W.: Impacts of the East](#)
934 [Asian winter monsoon and local sea surface temperature on heavy snowfall over the](#)
935 [Yeongdong region, *J. Clim.*, 32\(20\), 6783–6802, doi:10.1175/JCLI-D-18-0411.1. 2019.](#)

936 [Kim, T., and Jin, E. K.: Impact of an interactive ocean on numerical weather prediction:](#)
937 [A case of a local heavy snowfall event in eastern Korea, *J. Geophys. Res. Atmos.*, 121,](#)
938 [8243–8253, doi:10.1002/2016JD02476, 2016.](#)

939 [Ko, A.-R., Kim, B.-G., Eun, S.-H., Park, Y.-S. and Choi, B.-C.: Analysis of the](#)
940 [relationship of water vapor with precipitation for the winter ESSAY \(Experiment on](#)
941 [Snow Storms At Yeongdong\) period, *Atmosphere*, 26\(1\), 19–33,](#)
942 [doi:10.14191/atmos.2016.26.1.019, 2016.](#)

943 Kongoli, C., Meng, H., Dong, J. and Ferraro, R.: A snowfall detection algorithm over
944 land utilizing high-frequency passive microwave measurements—Application to ATMS,
945 *J. Geophys. Res.*, doi:10.1002/2014JD022427, 2015.

946 [Kneifel, S., Löhnert, U., Battaglia, A., Crewell, S. and Siebler, D.: Snow scattering](#)
947 [signals in ground-based passive microwave measurements. *J. Geophys. Res.*, 115,](#)
948 [D16214. doi:10.1029/2010JD013856, 2010.](#)

949 [Kneifel, S., Redl, S., Orlandi, E., Löhnert, U., Cadeddu, M. P., Turner, D. D., and Chen,](#)
950 [M.-T.: Absorption Properties of Supercooled Liquid Water between 31 and 225 GHz:](#)
951 [Evaluation of Absorption Models Using Ground-based Observations, *J. Appl. Meteor.*](#)
952 [Climatol., 53, 1028-1045. doi:10.1175/JAMC-D-13-0214.1, 2014.](#)

953 Kruger, A. and Krajewski, W. F.: Two-dimensional video disdrometer: A description, *J.*
954 *Atmos. Ocean. Technol.*, doi:10.1175/1520-0426(2002)019<0602:TDVDAD>2.0.CO;2,
955 2002.

956 [Küchler, N., Kneifel, S., Löhnert, U., Kollias, P., Czekala, H. and Rose, T.: A W-band](#)
957 [radar–radiometer system for accurate and continuous monitoring of clouds and](#)
958 [precipitation. *J. Atmos. Oceanic Technol.*, 34, 2375–2392. doi: 10.1175/JTECHD-17-](#)
959 [0019.1, 2017.](#)

960 Kulie, M. S. and Bennartz, R.: Utilizing spaceborne radars to retrieve dry Snowfall, *J.*
961 *Appl. Meteorol. Climatol.*, 48(12), 2564–2580, doi:10.1175/2009JAMC2193.1, 2009.

962 Kulie, M. S., Milani, L., Wood, N. B., Tushaus, S. A., Bennartz, R., L’Ecuyer, T. S. and
963 L’Ecuyer, T. S.: A shallow cumuliform snowfall census using spaceborne radar, *J.*

964 Hydrometeorol., 17(4), 1261–1279, doi:10.1175/JHM-D-15-0123.1, 2016.

965 Kummerow, C., Olson, W. S. and Giglio, L.: A simplified scheme for obtaining
966 precipitation and vertical hydrometeor profiles from passive microwave sensors, IEEE
967 Trans. Geosci. Remote Sens., doi:10.1109/36.536538, 1996.

968 Kummerow, C. D., Randel, D. L., Kulie, M., Wang, N. Y., Ferraro, R., Joseph Munchak,
969 S. and Petkovic, V.: The evolution of the goddard profiling algorithm to a fully
970 parametric scheme, J. Atmos. Ocean. Technol., doi:10.1175/JTECH-D-15-0039.1, 2015.

971 [Liebe, H. J., Hufford, G. A., and Cotton, M. G.: Propagation modeling of moist air and](#)
972 [suspended water/ice particles at frequencies below 1000 GHz, AGARD Conf.](#)
973 [Proc.,542,3-1-3-10,1993.](#)

974 Liu, G.: A fast and accurate model for microwave radiance calculations, J. Meteorol. Soc.
975 Japan, doi:10.2151/jmsj1965.76.2_335, 1998.

976 Liu, G.: Approximation of Single Scattering Properties of Ice and Snow Particles for
977 High Microwave Frequencies, J. Atmos. Sci., 61(20), 2441–2456, doi:10.1175/1520-
978 0469(2004)061<2441:AOSPO>2.0.CO;2, 2004.

979 Liu, G.: Deriving snow cloud characteristics from CloudSat observations, J. Geophys.
980 Res. Atmos., 114(8), 1–13, doi:10.1029/2007JD009766, 2008a.

981 Liu, G.: A database of microwave single-scattering properties for nonspherical ice
982 particles, Bull. Am. Meteorol. Soc., 89(10), 1563–1570, doi:10.1175/2008BAMS2486.1,
983 2008b.

984 Liu, G. and Curry, J. A.: Precipitation characteristics in Greenland-Iceland-Norwegian
985 Seas determined by using satellite microwave data and modeling studies that require
986 Observations Salinity satellite retrievals are the only platform from described by Schmitt
987 cycle for tropical , , 102, 987–997, 1997.

988 Liu, G. and Seo, E.-K. K.: Detecting snowfall over land by satellite high-frequency
989 microwave observations: The lack of scattering signature and a statistical approach, J.
990 Geophys. Res. Atmos., 118(3), 1376–1387, doi:10.1002/jgrd.50172, 2013.

991 Liu, G. and Takeda, T.: Interesting findings on the precipitation of middle-level
992 stratiform clouds in recent years are a banded mesoscale structure of rainfall and a
993 showed that precipitation is initiated in high-level clouds (" seeder " clouds) and it is
994 enhanced in deep stra, , (October), 645–660, 1988.

995 Locatelli, J. D. and Hobbs, P. V.: Fall speeds and masses of solid precipitation particles,
996 J. Geophys. Res., doi:10.1029/jc079i015p02185, 1974.

997 Löffler-Mang, M. and Joss, J.: An optical disdrometer for measuring size and velocity of
998 hydrometeors, J. Atmos. Ocean. Technol., doi:10.1175/1520-
999 0426(2000)017<0130:AODFMS>2.0.CO;2, 2000.

1000 Marchand, R., Mace, G. G., Ackerman, T. and Stephens, G.: Hydrometeor detection
1001 using Cloudsat - An earth-orbiting 94-GHz cloud radar, J. Atmos. Ocean. Technol.,
1002 25(4), 519–533, doi:10.1175/2007JTECHA1006.1, 2008.

1003 Meng, H., Dong, J., Ferraro, R., Yan, B., Zhao, L., Kongoli, C., Wang, N. Y. and
1004 Zavodsky, B.: A 1DVAR-based snowfall rate retrieval algorithm for passive microwave
1005 radiometers, J. Geophys. Res., 122(12), 6520–6540, doi:10.1002/2016JD026325, 2017.

1006 [Nam, H. G., Kim, B. G., Han, S. O., Lee, C. and Lee, S. S.: Characteristics of easterly-](#)
1007 [induced snowfall in Yeongdong and its relationship to air-sea temperature difference,](#)
1008 [Asia-Pacific J. Atmos. Sci., 50\(4\), 541–552, doi:10.1007/s13143-014-0044-3, 2014.](#)

1009 Noh, Y. J., Liu, G., Seo, E. K., Wang, J. R. and Aonashi, K.: Development of a snowfall
1010 retrieval algorithm at high microwave frequencies, J. Geophys. Res. Atmos.,
1011 doi:10.1029/2005JD006826, 2006.

1012 Olson, W. S., Kummerow, C. D., Heymsfield, G. M. and Giglio, L.: A method for
1013 combined passive-active microwave retrievals of cloud and precipitation profiles, J.
1014 Appl. Meteorol., 35(10), 1763–1789, doi:10.1175/1520-
1015 0450(1996)035<1763:AMFCPM>2.0.CO;2, 1996.

1016 [Park, H., Lee, J., Chang, E.: High-resolution simulation of snowfall over the Korean](#)
1017 [eastern coastal pegin using WRF model: Sensitivity to domain nesting-down strategy.](#)
1018 [Asia-Pacific J. Atmos. Sci. 55, 493–506. https://doi.org/10.1007/s13143-019-00108-x,](#)

1019 [2019.](#)

1020 [Pettersen, C., Kulie, M. S., Bliven, L. F., Merrelli, A. J., Petersen, W. A., Wagner, T. J.,](#)
1021 [Wolff, D. B., and Wood, N. B: A composite analysis of snowfall modes from four winter](#)
1022 [seasons in Marquette, Michigan. J. Appl. Meteor. Climatol., 59\(1\), 103-124, 2020,](#)
1023 [doi:/10.1175/JAMC-D-19-0099.1, 2020.](#)

1024 [Pettersen, C., Bennartz, R., Merrelli, A. J., Shupe, M. D., Turner, D. D., and Walden, V.](#)
1025 [P.: Precipitation regimes over central Greenland inferred from 5 years of ICECAPS](#)
1026 [observations. Atmos. Chem. Phys., 18, 4715-4735. doi:/10.5194/acp-18-4715-2018,](#)
1027 [2018.](#)

1028 [Rosenkranz, P. W.: Water vapor microwave continuum absorption: A comparison of](#)
1029 [measurements and models. Radio Sci., 33, 919-928, 1998.](#)

1030 RPG-FMCW: RPG-FMCW-94-SP/DP 94 GHz W-band Cloud Doppler Radar Instrument
1031 Installation, Operation and Software Guide (Version 2.10-1). [online] Available from:
1032 [https://www.radiometer-physics.de/downloadftp/pub/PDF/Cloud Radar/RPG-FMCW-](https://www.radiometer-physics.de/downloadftp/pub/PDF/Cloud%20Radar/RPG-FMCW-Instrument_Manual.pdf)
1033 [Instrument_Manual.pdf](https://www.radiometer-physics.de/downloadftp/pub/PDF/Cloud Radar/RPG-FMCW-Instrument_Manual.pdf) (Accessed 22 January 2020), 2015.

1034 Praz, C., Roulet, Y. A. and Berne, A.: Solid hydrometeor classification and riming degree
1035 estimation from pictures collected with a Multi-Angle Snowflake Camera, Atmos. Meas.
1036 Tech., doi:10.5194/amt-10-1335-2017, 2017.

1037 [Schwartz, M. J.: Observation and Modeling of Atmospheric Oxygen Millimeter-Wave](#)
1038 [Transmittance. Ph.D. Thesis, Massachusetts Institute of Technology, Department of](#)
1039 [Physics, 1998.](#)

1040 Sekhon, R. S. and Srivastava, R. C.: Doppler radar observations of drop- size
1041 distributions in a thunderstorm, J. Atmos. Sci., 28(6), 983–994, 1971.

1042 Seo, E. K. and Liu, G.: Retrievals of cloud ice water path by combining ground cloud
1043 radar and satellite high-frequency microwave measurements near the ARM SGP site, J.
1044 Geophys. Res. D Atmos., 110(14), 1–15, doi:10.1029/2004JD005727, 2005.

1045 Sims, E. M. and Liu, G.: A parameterization of the probability of snow-rain transition, J.
1046 Hydrometeorol., 16(4), 1466–1477, doi:10.1175/JHM-D-14-0211.1, 2015.

1047 Skofronick-Jackson, G. and Johnson, B. T.: Surface and atmospheric contributions to
1048 passive microwave brightness temperatures for falling snow events, *J. Geophys. Res.*
1049 *Atmos.*, 116(2), 1–16, doi:10.1029/2010JD014438, 2011.

1050 Skofronick-Jackson, G., Petersen, W. A., Berg, W., Kidd, C., Stocker, E. F., Kirschbaum,
1051 D. B., Kakar, R., Braun, S. A., Huffman, G. J., Iguchi, T., Kirstetter, P. E., Kummerow,
1052 C., Meneghini, R., Oki, R., Olson, W. S., Takayabu, Y. N., Furukawa, K. and Wilheit, T.:
1053 The Global Precipitation Measurement (GPM) Mission for Science and Society, *Bull.*
1054 *Am. Meteorol. Soc.*, 98(8), 1679–1695, doi:10.1175/BAMS-D-15-00306.1, 2017.

1055 Skofronick-Jackson, G. M., Weinman, J. A., Kim, M. J. and Chang, D. E.: A physical
1056 model to determine snowfall over land by microwave radiometry, *IEEE Trans. Geosci.*
1057 *Remote Sens.*, 42(5), 1047–1058, doi:10.1109/TGRS.2004.825585, 2004.

1058 Stephens, G. L., Austin, R. T., Benedetti, A., Mitrescu, C., Vane, D. G., Boain, R. J.,
1059 Durden, S. L., Mace, G. G. J., Sassen, K., Wang, Z., Illingworth, A. J., O’Connor, E. J.,
1060 Rossow, W. B. and Miller, S. D.: The cloudsat mission and the A-Train: A new
1061 dimension of space-based observations of clouds and precipitation, *Bull. Am. Meteorol.*
1062 *Soc.*, 83(12), 1771-1790+1742, doi:10.1175/BAMS-83-12-1771, 2002.

1063 Tanelli, S., Durden, S. L., Im, E., Pak, K. S., Reinke, D. G., Partain, P., Haynes, J. M. and
1064 Marchand, R. T.: CloudSat’s cloud profiling radar after two years in orbit: Performance,
1065 calibration, and processing, *IEEE Trans. Geosci. Remote Sens.*, 46(11), 3560–3573,
1066 doi:10.1109/TGRS.2008.2002030, 2008.

1067 Tang, G., Wen, Y., Gao, J., Long, D., Ma, Y., Wan, W. and Hong, Y.: Similarities and
1068 differences between three coexisting spaceborne radars in global rainfall and snowfall
1069 estimation, *Water Resour. Res.*, 53(5), 3835–3853, doi:10.1002/2016WR019961, 2017.

1070 Tokay, A., Wolff, D. B. and Petersen, W. A.: Evaluation of the new version of the laser-
1071 optical disdrometer, OTT parsivel, *J. Atmos. Ocean. Technol.*, doi:10.1175/JTECH-D-
1072 13-00174.1, 2014.

1073 [Wang, Y., Chen, Y., Fu, F., and Liu, G.: Identification of precipitation onset based on](#)
1074 [CloudSat observations. *J. Quant. Spect. Radiat. Trans.*, 188, 142-177.](#)

1075 [doi:10.1016/j.jqsrt.2016.06.028](https://doi.org/10.1016/j.jqsrt.2016.06.028), 2017.

1076 Wang, Y., Liu, G., Seo, E. K. and Fu, Y.: Liquid water in snowing clouds: Implications
 1077 for satellite remote sensing of snowfall, *Atmos. Res.*, 131, 60–72,
 1078 doi:10.1016/j.atmosres.2012.06.008, 2013.

1079 Wood, N. B., L’Ecuyer, T. S., Vane, D. G., Stephens, G. L. and Partain, P.: Level 2C
 1080 snow profile process description and interface control document, version 0, CloudSat
 1081 Proj., (D), 21 [online] Available from: [http://www.cloudsat.cira.colostate.edu/ICD/2C-](http://www.cloudsat.cira.colostate.edu/ICD/2C-SNOW-PROFILE/2C-SNOW-PROFILE_PDICD_P_R04.pdf)
 1082 [SNOW-PROFILE/2C-SNOW-PROFILE_PDICD_P_R04.pdf](http://www.cloudsat.cira.colostate.edu/ICD/2C-SNOW-PROFILE/2C-SNOW-PROFILE_PDICD_P_R04.pdf), 2013.

1083 [Ye, B.-Y.](#), [Jung, E.](#), [Shin, S.](#) and [Lee, G.](#): Statistical Characteristics of Cloud Occurrence
 1084 and Vertical Structure Observed by a Ground-Based Ka-Band Cloud Radar in South
 1085 Korea. *Remote Sens.*, 12, 2242, doi:10.3390/rs12142242, 2020.

1086 Yin, M. and Liu, G.: Developing an a priori database for passive microwave snow water
 1087 retrievals over ocean, *J. Geophys. Res. Atmos.*, 122(23), 12,960-12,981,
 1088 doi:10.1002/2017JD027636, 2017.

1089 Yin, M. and Liu, G.: Assessment of GPM high-frequency microwave measurements with
 1090 radiative transfer simulation under snowfall conditions, *Q. J. R. Meteorol. Soc.*,
 1091 145(721), 1603–1616, doi:10.1002/qj.3515, 2019.

1092 Yuter, S. E. and Houze, R. A.: Three-Dimensional Kinematic and Microphysical
 1093 Evolution of Florida Cumulonimbus. Part II: Frequency Distributions of Vertical
 1094 Velocity, Reflectivity, and Differential Reflectivity, *Mon. Weather Rev.*, 123(7), 1941–
 1095 1963, doi:10.1175/1520-0493(1995)123<1941:tdkame>2.0.co;2, 1995.

1096 Zhang, J., Howard, K., Langston, C., Kaney, B., Qi, Y., Tang, L., Grams, H., Wang, Y.,
 1097 Cocks, S., Martinaitis, S., Arthur, A., Cooper, K., Brogden, J. and Kitzmiller, D.: Multi-
 1098 Radar Multi-Sensor (MRMS) Quantitative Precipitation Estimation: Initial Operating
 1099 Capabilities, *Bull. Am. Meteorol. Soc.*, 97(4), 621–638, doi:10.1175/BAMS-D-14-
 1100 00174.1, 2016.

1101
 1102

Deleted ;

Deleted ;

Deleted ;

Formatted: Font: (Default) Times New Roman, 12 pt, Font color: Green

Formatted: Font: (Default) Times New Roman, 12 pt, Font color: Auto

Formatted: Font color: Auto

Formatted: Font color: Auto

Formatted: Font color: Auto

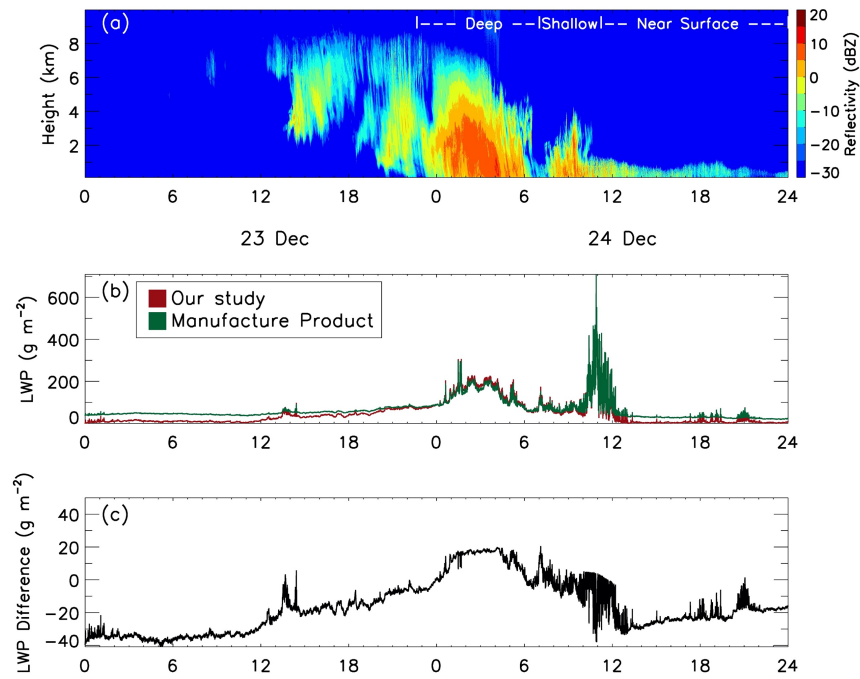
Formatted: Font color: Auto

Formatted: Font: (Default) Times New Roman, 12 pt, Font color: Auto

Formatted: Font: (Default) Times New Roman, 12 pt

Formatted: Font: (Default) Times New Roman, 12 pt, Font color: Auto

Formatted: Font color: Green



1106

1107

1108

1109

1110 Fig.1 (a) Radar reflectivity, (b) two liquid water path retrievals and (c) their differences

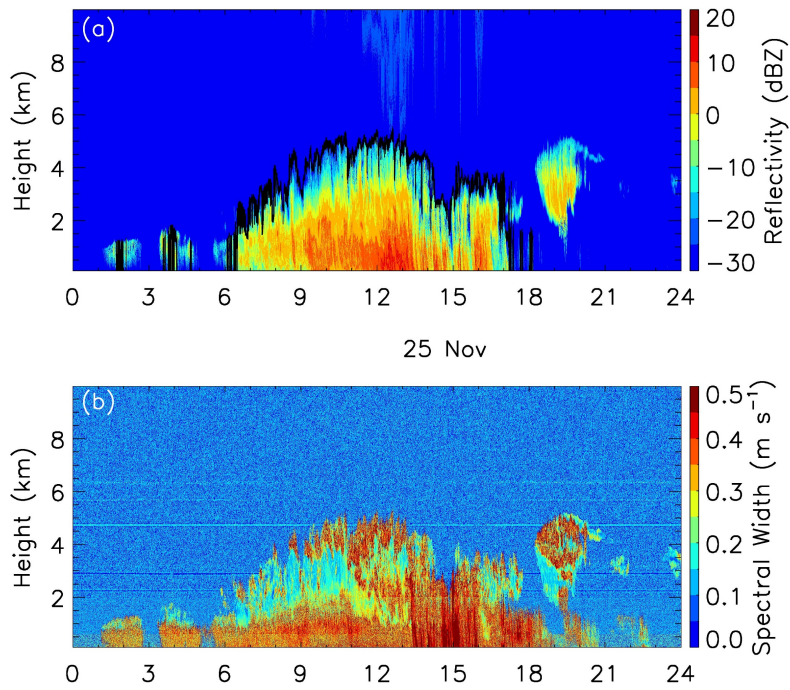
1111 (LWP of our study plus manufacture product) for observations during 23 and 24

1112 December 2017. In the top panel, cloud types as defined in the text are also indicated.

1113

1114

1115



1116

1117

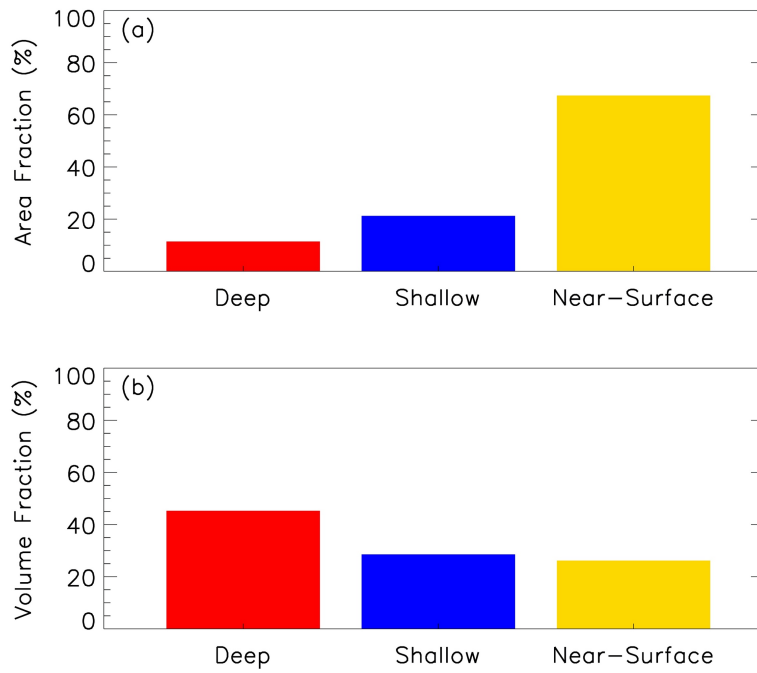
1118

1119

1120 Fig.2 Height-time cross section of (a) radar reflectivity and (b) Doppler spectral width for
1121 observations on 25 November 2017. The cloud top for snowing clouds (surface radar
1122 reflectivity greater than -20 dBZ) is also shown in the top panel.

1123

1124



1125

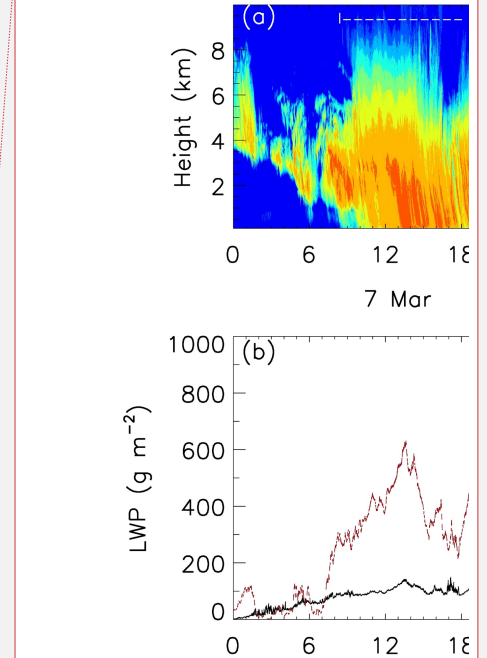
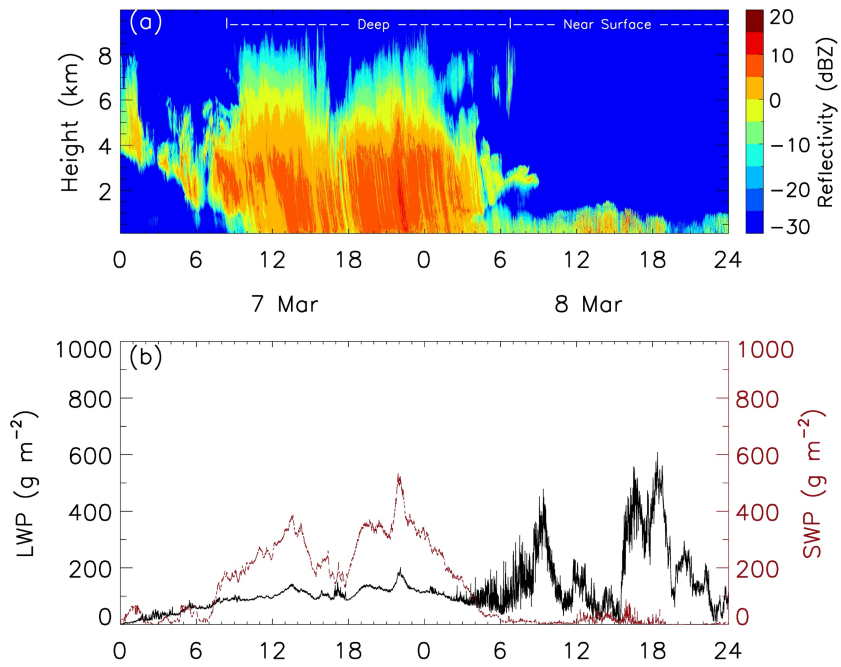
1126

1127

1128 Fig.3 (a) Area and (b) volume fractions of the 3 types of snowing clouds observed during
 1129 the 2017-18 winter season.

1130

1131



Deleted:

1132

1133

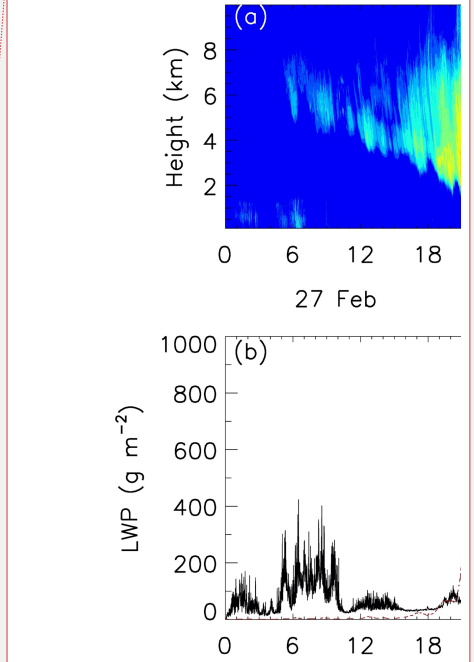
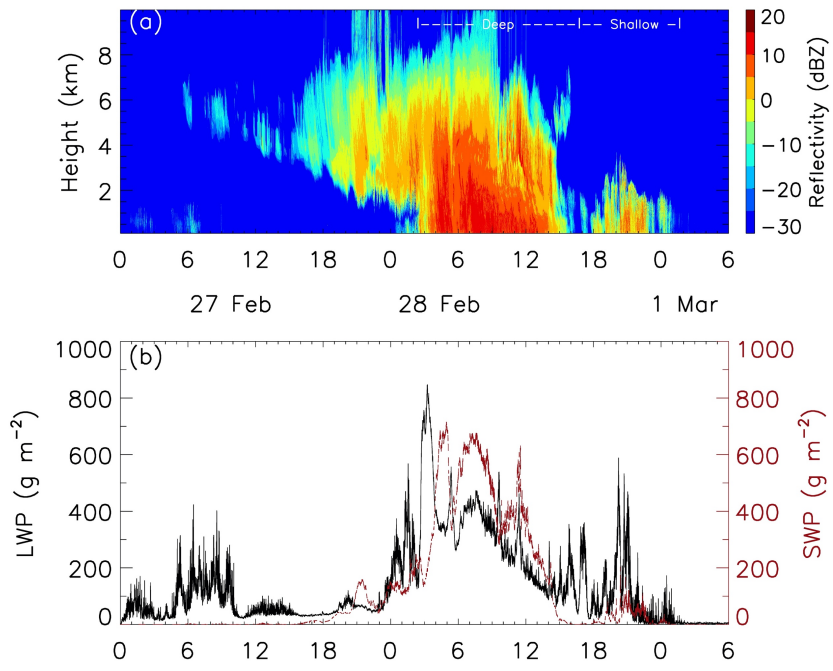
1134

1135 Fig.4 (a) Height-time cross section of radar reflectivity and (b) time series of liquid water

1136 path (LWP, black) and snow water path (SWP, red) for observations on 7 and 8 March

1137 2018.

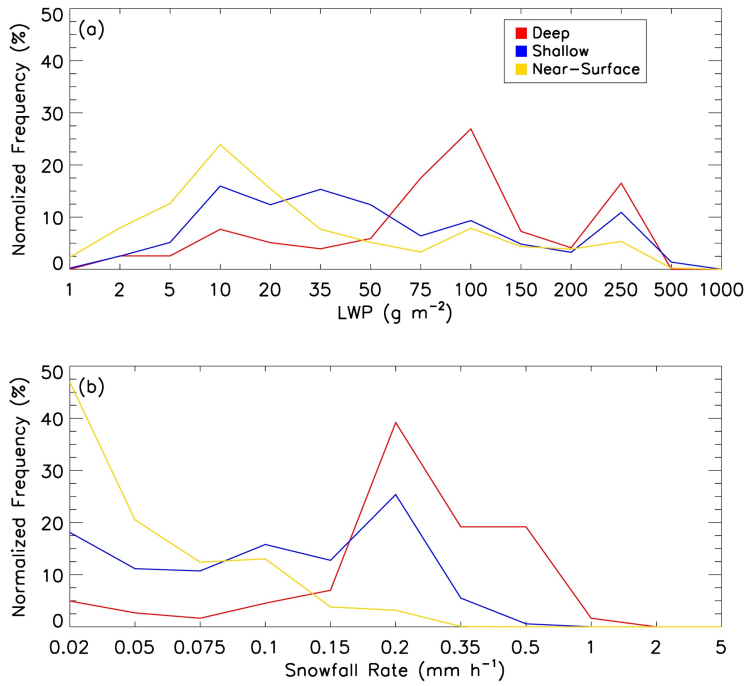
1138



Deleted:

1140
1141
1142
1143
1144
1145
1146
1147
1148

Fig.5 (a) Height-time cross section of radar reflectivity and (b) time series of liquid water path (LWP, black) and snow water path (SWP, red) for observations from 27 February through 1 March 2018.



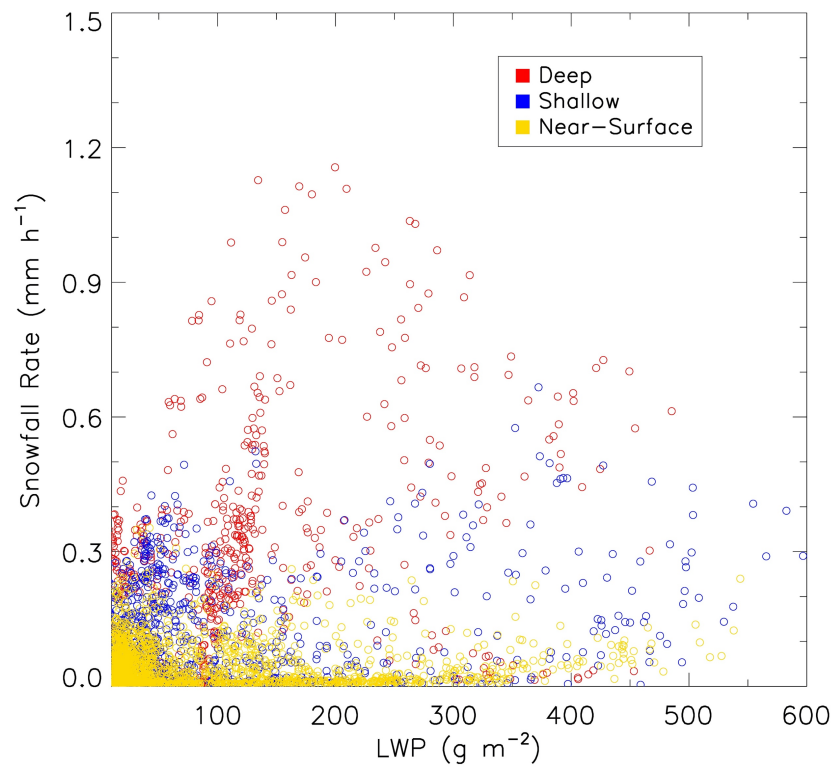
1150

1151

1152

1153 Fig.6 Frequency distribution of (a) liquid water path and (b) snowfall rate at surface
 1154 derived from all observed snowfall data during the 2017-18 winter. The frequency values
 1155 are normalized so that the sum of their values at all bins is 100%.

1156



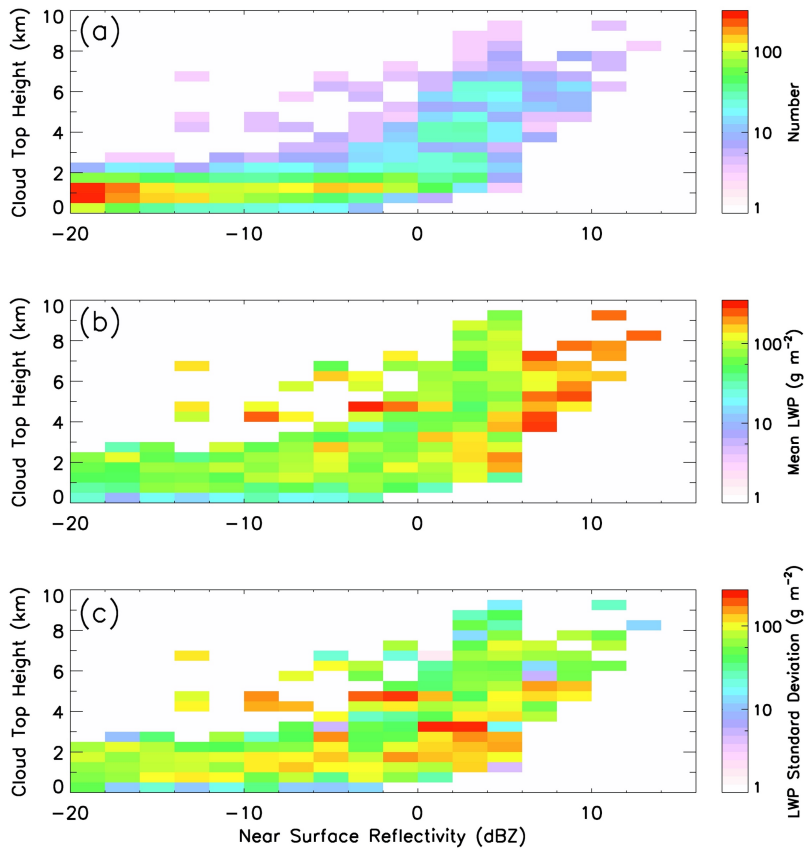
1157

1158

1159 Fig.7 Scatterplot of liquid water path and surface snowfall rate. Each point is an average
1160 of 5-minute data. All observed data during the 2017-18 winter are included.

1161

1162

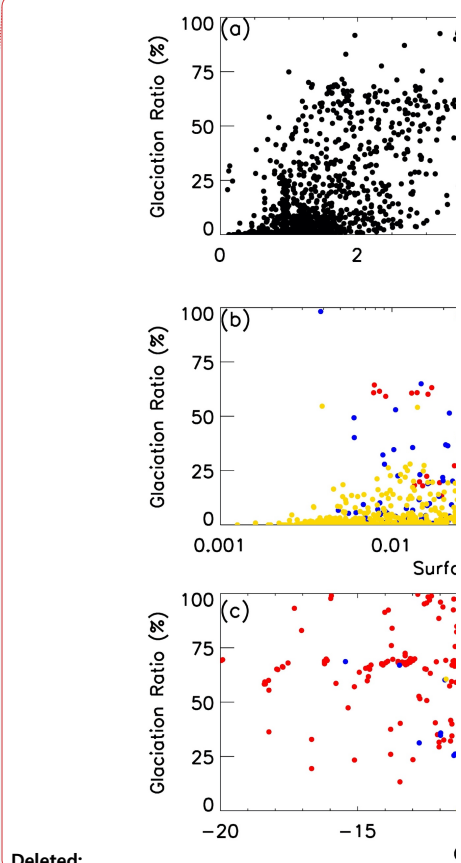
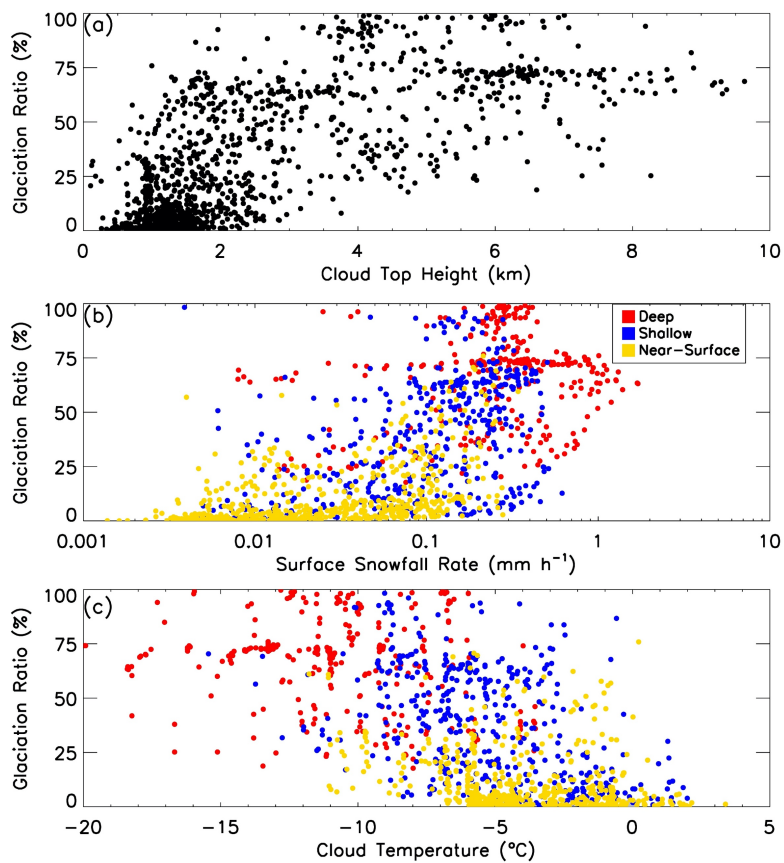


1163

1164

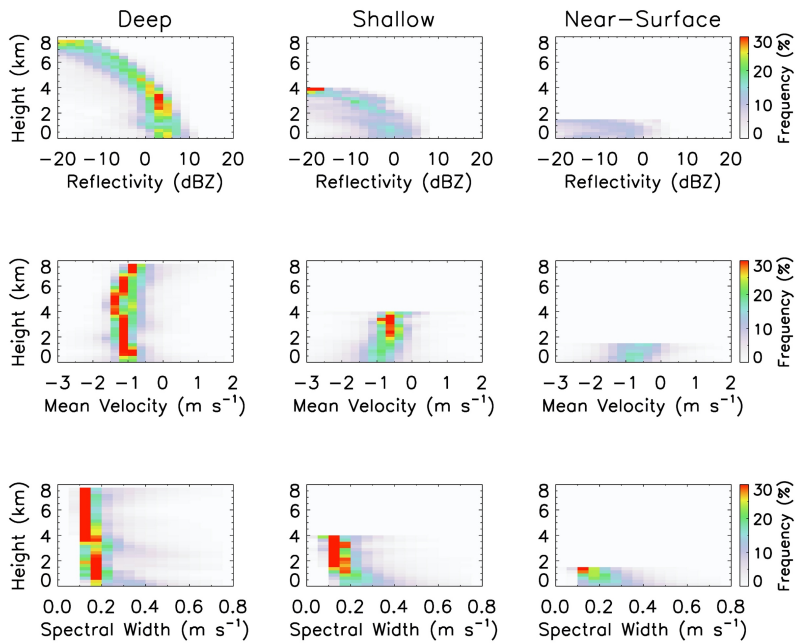
1165 Fig.8 Two-dimensional distributions of (a) number of occurrences, (b) liquid water path
 1166 and (c) standard deviation of liquid water path as a function of near surface radar
 1167 reflectivity and cloud top height. All observed data during the 2017-18 winter are used in
 1168 calculate the distributions.

1169



1170
1171
1172

1173 Fig.9 Scatterplot of glaciation ratio (see definition in the text) with (a) cloud top height,
1174 (b) surface snowfall rate and (c) cloud temperature based on 5-minute averages of all
1175 observational data of snowing clouds in the 2017-18 winter.



1177

1178

1179

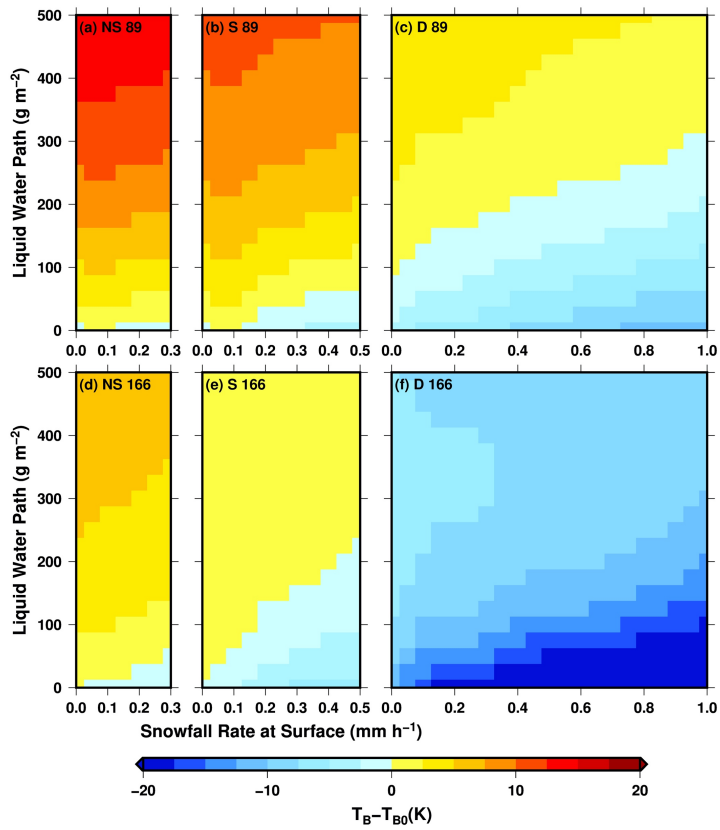
1180 Fig.10 Contoured frequency by altitude diagram (CFADs) for radar reflectivity (top),
 1181 mean Doppler velocity (middle) and Doppler spectral width (bottom) for deep (left),
 1182 shallow (middle) and near-surface (right) snowing clouds. The frequency values are
 1183 calculated in such a way that the sum of all frequency values at each altitude is 100%. All
 1184 observed data from the 2017-18 winter are used.

1185

1186

1187

1188



1189

1190 Fig.11 Simulated brightness temperature change (relative to clear-sky) at GMI 89 GHz
 1191 (top) and 166 GHz (bottom) for near-surface (left), shallow (middle) and deep (right)
 1192 snowing clouds. The change is relative to values at clear-sky.

1193

1194

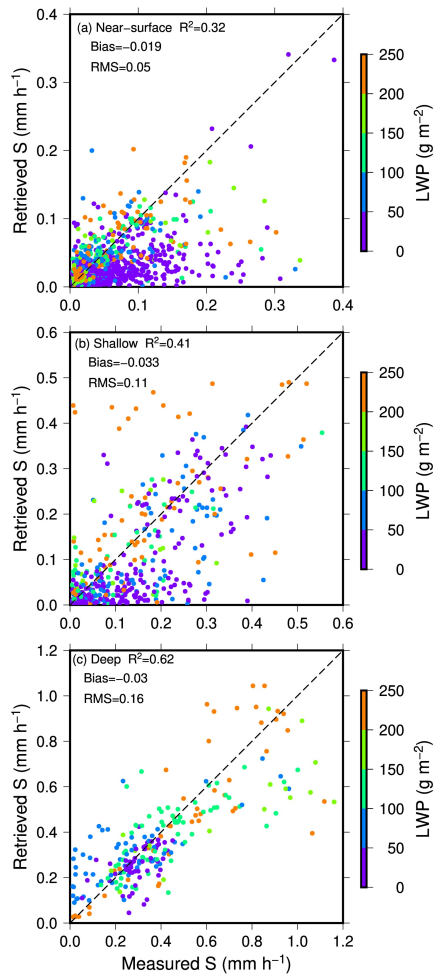
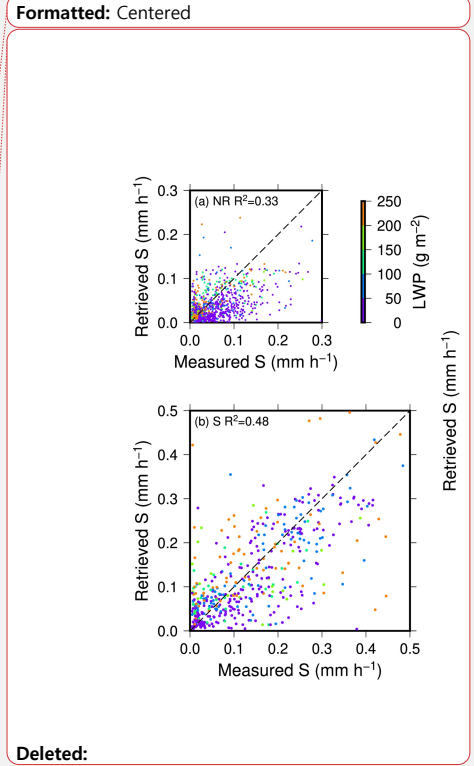


Fig.12

1195
1196
1197
1198
1199
1200

Scatterplot of “measured” versus “retrieved” snowfall rate for (a) near-surface, (b) shallow and (c) deep snowing clouds over land. Color of the points indicates liquid water path associated with the case. Correlation is indicated by R^2 in each diagram. Biases and root-mean-square (RMS) differences are also indicated in the diagrams.



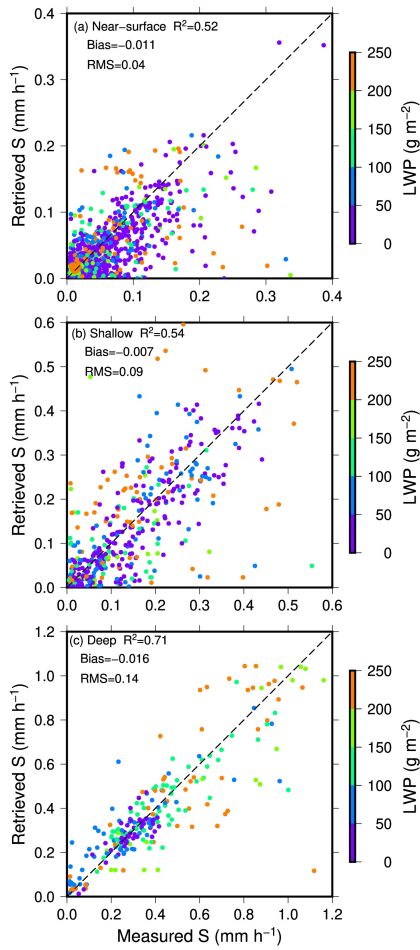


Fig.13

1203

1204

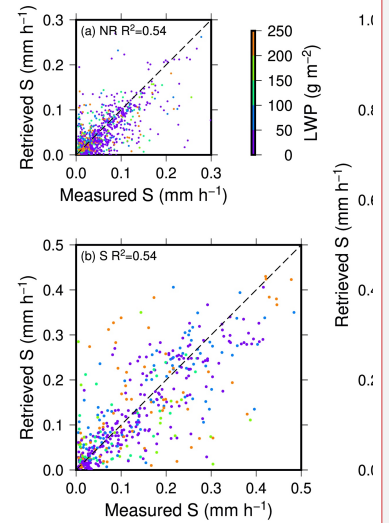
1205

1206

1207

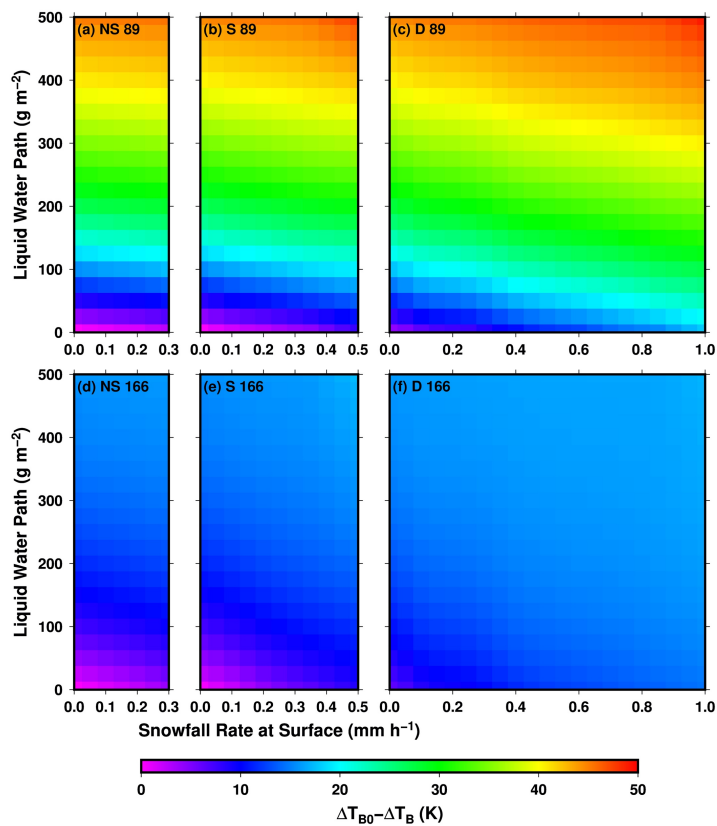
Scatterplot of “measured” versus “retrieved” snowfall rate for (a) near-surface, (b) shallow and (c) deep snowing clouds over ocean. Color of the points indicates liquid water path associated with the case. Correlation is indicated by R^2 in each diagram. Biases and root-mean-square (RMS) differences are also indicated in the diagrams.

Formatted: Centered, Don't adjust right indent when grid is defined, Line spacing: 1.5 lines, No widow/orphan control, Don't adjust space between Latin and Asian text, Don't adjust space between Asian text and numbers



Deleted:

Deleted: ¶
.....Page Break.....



1211

1212 Fig.14 Simulated change of depolarization for GMI 89 GHz (top) and 166 GHz (bottom)

1213 for near-surface (left), shallow (middle) and deep (right) snowing clouds over ocean.

1214 Depolarization is the brightness temperature difference between vertical and horizontal

1215 polarizations. The change is relative to values at clear-sky.

1216